The applicability of heat flux sensors in a falling film evaporator: Experimental approach

R.C.A. Cornel

Technische Universiteit Delft

TU Delft

The applicability of heat flux sensors in a falling film evaporator: Experimental approach

by

R.C.A. Cornel

to obtain the degree of Master of Science
at the Delft University of Technology,
to be defended publicly on Thursday July 19, 2018 at 14:00 PM.

Report number:	2899	
Student number:	4106083	
Project duration:	March, 2017 – July, 2018	
Thesis committee:	Prof. dr. ir. B.J. Boersma,	TU Delft, supervisor
	Dr. R. Delfos,	TU Delft, supervisor
	Prof. dr. ir. W. de Jong,	TU Delft
	Ir. F. Jacobs,	FrieslandCampina
	Ing. G. van Gils,	FrieslandCampina
	D. Badloe PDEng,	FrieslandCampina

An electronic version of this thesis is available at `http://repository.tudelft.nl/`.

TU Delft

Acknowledgements

This thesis gave me the opportunity to get insight into the fluid and heat challenges that companies face in practice. Furthermore, performing calculations and building an experimental setup from scratch was something which had my interest from the beginning onwards.

Of course, I could not have done this research without the support of numerous persons to whom I am very grateful to. First of all, I want to thank FrieslandCampina for initiating this project and in particular ir. Fons Jacobs, ing. Gerard van Gils and Dinesh Badloe PDEng. Their support during this project, from the start of this project, the insight in this problem which I have been facing, to the end of the project to have constructive comments to improve the analysis of the results helped me a lot. I am also grateful that the results are shared within FrieslandCampina by the meaning of a presentation. It shows that the problem is significant and I am glad to be part of this process. I also want to thank both supervisors. Prof. dr. ir. Bendiks Jan Boersma for always making time for discussions and guiding me during this project. Dr. René Delfos for evaluating the performed calculations, discussing the obtained results and for teaching me the importance of exact formulations which greatly helped me better explain the problems. I would like to thank prof. dr. ir. Wiebren de Jong for participating in my thesis committee. For the support by constructing the experimental setup, I would like to thank DEMO, and in particular Jaap van Raamt for discussing the possibilities for the setup and for arranging a suitable location in the process hall, Martijn Karsten for installing the electrical components and Daniel van Baarle for helping me out with the mechanical work.

R.C.A. Cornel
Delft, July 2018

Abstract

The production process of milk powder consists of multiple stages. This report focuses on the falling film evaporator, which role in the production process is to evaporate the water content from the milk. A falling film evaporator is a large vertically-placed vessel whereby the inside is filled with smaller tubes. Steam enters the vessel and heats up the outside of the smaller tubes. The milk flows in a thin layer only along the inside perimeter of the smaller tubes, so these tubes are not completely filled. The advantage of this flow is that a thin layer of liquid is continuously in contact with the wall so the heating process is equal along the tube. The thin layer is called a falling film because the thickness compared to the length of the flow is very small.

The objective of this research is to determine theoretically the local overall heat transfer coefficient of the falling film and to investigate experimentally the applicability of heat flux sensors by determining the local overall heat transfer coefficient. By investigating the falling film, it is not allowed to disturb the falling film. Once a falling film is disturbed, the falling film will proceed at a different path. Heat flux sensors allow for local non-intrusive measurements. The overall heat transfer coefficient gives information about the thickness of the falling film. Theoretically the overall heat transfer coefficient is calculated by taken the thermal resistances of each component. Experimentally, the overall heat transfer coefficient is measured by the heat flux and the temperature difference between the bulk temperature of the fluid and the sensor at the outside of the tube.

Before the heat flux sensors are used in practice on the falling film evaporator, a setup has been built to experimentally determine the applicability of the heat flux sensor. This setup has been made for a tube filled with water and to create a falling film. The tube filled with water is well-described in theory and used as a reference.

The results of the experimental setup show that the Danfoss 'Koperpasta tube AT' is in good comparison with the theoretical approach. The theoretical overall heat transfer coefficient difference, caused by the mass flow difference of 0.01 kg/s in the falling film evaporator, can be detected by the heat flux sensors taking into account the error margin of the heat flux sensor and temperature sensor.

Nomenclature

Dimensionless numbers

Gr	Grashof number	-
Ja	Jakob number	-
Nu	Nusselt number	-
Pr	Prandtl number	-
Ra	Rayleigh number	-
Re	Reynolds number	-

Greek Symbols

α_s	Seebeck coefficient	$V\,K^{-1}$
β	Thermal expansion coefficient	K^{-1}
δ	Thickness of film	m
ϵ	Relative roughness	m
Γ	Mass flow per unit width	$kg\,m^{-1}\,s^{-1}$
μ	Kinematic viscosity	$m^2\,s^{-1}$
ν	Dynamic viscosity	Pa s
ρ	Density	$kg\,m^{-3}$
τ_w	Shear stress	Pa

Roman Symbols

ΔV	Voltage	V
$\dot{m}''$	Evaporation rate	$kg\,m^{-2}\,s^{-1}$
$\dot{Q}$	Rate of heat transfer	W
$\hat{n}$	Unit vector	-
∇	Nabla	-
A	Area	m^2
A_c	Cross sectional area	m^2
c_p	Heat capacity	$J\,kg^{-1}\,K^{-1}$
D	Diameter	m

D_h	Hydraulic diameter	m
f	Friction factor	-
g	Gravity	m s^{-2}
h_c	Convective heat transfer coefficient	W m^{-2} K^{-1}
h_f	Head loss	m
h_l, h_g	Enthalpy liquid, vapour	J
h_r	Radiative heat transfer coefficient	W m^{-2} K^{-1}
h_{fg}	Enthalpy phase change	J
K	Loss coefficient	-
k	Thermal conductivity	W m^{-1} K^{-1}
P	Pressure	Pa
P_m	Perimeter	m
q	Heat flux	W m^{-2}
S	Mass fraction	%
T	Temperature	K
U	Overall heat transfer coefficient	W m^{-2} K^{-1}
u	Velocity	m s^{-1}
V	Volume	m^3
x, L	Distance	m
z	Height	m

Contents

1 Introduction **1**
- 1.1 Processing milk powder . . . 1
- 1.2 Falling film evaporator . . . 4
- 1.3 Research outline . . . 8

2 Theory **9**
- 2.1 Principle of heat transfer . . . 9
- 2.2 Falling film . . . 10
- 2.3 Heat transfer in falling film . . . 11
  - 2.3.1 Fluid dynamics . . . 11
  - 2.3.2 Heat transfer . . . 13
  - 2.3.3 Relation between the Nusselt number and Reynolds number . . . 14
  - 2.3.4 Properties milk in falling film . . . 15
- 2.4 Full flow water . . . 16
  - 2.4.1 Pressure loss . . . 16
  - 2.4.2 Thermal phenomena in full flow tube . . . 18
  - 2.4.3 Heat transfer full flow water . . . 21

3 Experimental setup **23**
- 3.1 Components in experimental setup . . . 23
  - 3.1.1 Selection of cooling system . . . 24
  - 3.1.2 Selection of pump and flow meter . . . 25
  - 3.1.3 Creating a falling film . . . 25
  - 3.1.4 Heat flux sensor . . . 26
  - 3.1.5 Thermal paste . . . 28
- 3.2 Measurement area . . . 28
  - 3.2.1 Insulation . . . 29
- 3.3 Construction of the setup . . . 30
- 3.4 Heat transfer in measuring area . . . 32
- 3.5 Signal noise . . . 32

4 Results **35**
- 4.1 Falling film evaporator: theoretical approach . . . 35
- 4.2 Heat flux sensors: Experimental approach . . . 38
  - 4.2.1 Variable 1: Power input . . . 38
  - 4.2.2 Variable 2: Thermal paste . . . 42
  - 4.2.3 Variable 3: Change of position . . . 45
  - 4.2.4 Variable 4: Honeycomb structure . . . 46
  - 4.2.5 Theoretical curve . . . 47
  - 4.2.6 Reliability of experiments . . . 49

5 Conclusion **53**

6 Recommendations **55**

A Heat flux sensor specification **57**

Bibliography **59**

1 Introduction

1.1. Processing milk powder

Milk powder is used in many products and is transported to many countries all over the world. In contrary to milk, the powder has longer shelf life date and more compact volume. The largest producers of whole milk powder are Brazil, China, the European Union and New Zealand (fig. 1.1). The total amount produced for the year 2018 is estimated at 4,9 million metric tons. For non-fat milk powder, the production is estimated in the same order. The use of whole milk or non-fat milk depends on the priority per country.

The production process of milk powder starts with the evaporation of condensed milk. This type of milk is known for over one and a half century and was first patented by Gail Borden in 1853 after experimenting for more than ten years[1]. After that time, many other processes have been investigated for making the condensed milk such as condensation by refrigeration, by centrifugal force and by piling under atmospheric pressure. In the 1880's unsweetened condensed milk appeared for the first time on the market, introduced by John B. Meyenberg, who claimed his own patent in 1884.

Milk powder was developed by Grimwade in the same period as condensed milk but perfectionized in the last part of the nineteenth century and the beginning of the twentieth century. The main difference between condensed milk and milk powder is the degree of concentration. The commercial breakthrough of milk powder was around the first World War. During that time there where three dominating principles to make the milk powder, namely dough-drying, film-drying and spray drying [1]. Nowadays most common used method is the spray drying, because of the excellent solubility, flavour and colour [2].

[1] Three years later the claim stated the following words: "Producing concentrated sweet milk by evaporation in vacuo, substantially as set forth, the same having no sugar or other foreign matter mixed with it", United States Patent No. 15.553, August 19, 1856.

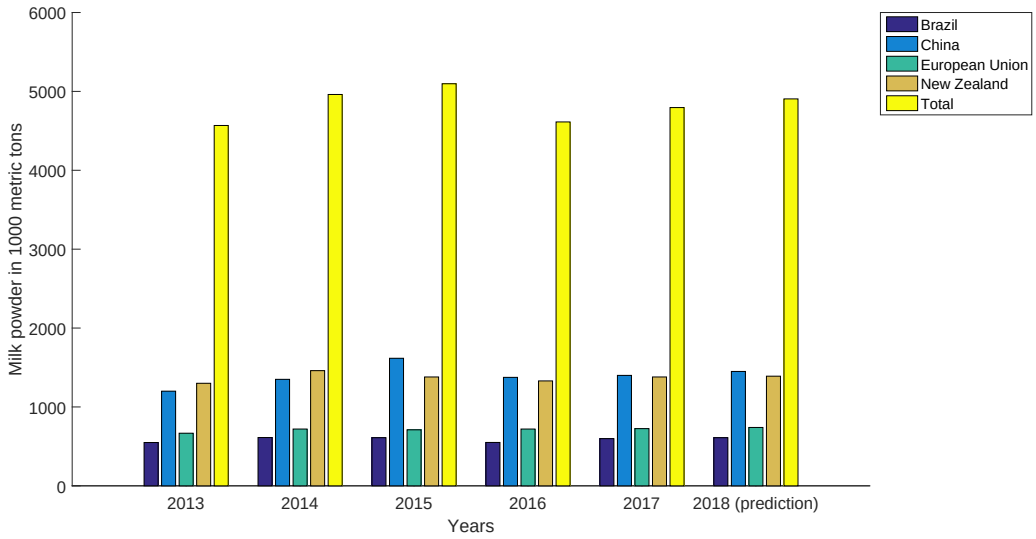

Figure 1.1: Production milk powder world wide [3]. The bars of 2018 are a prediction.

Multiple processes have to be performed to produce the milk powder, see figure 1.2. From left to right, the milk is stored in a milk silo before entering into the centrifuge. The skim milk is poured into a homogenizer and is pasteurized afterwards. Before the milk is flowing into the evaporator, the milk is preheated. The milk powder is created in the drier after the evaporator.

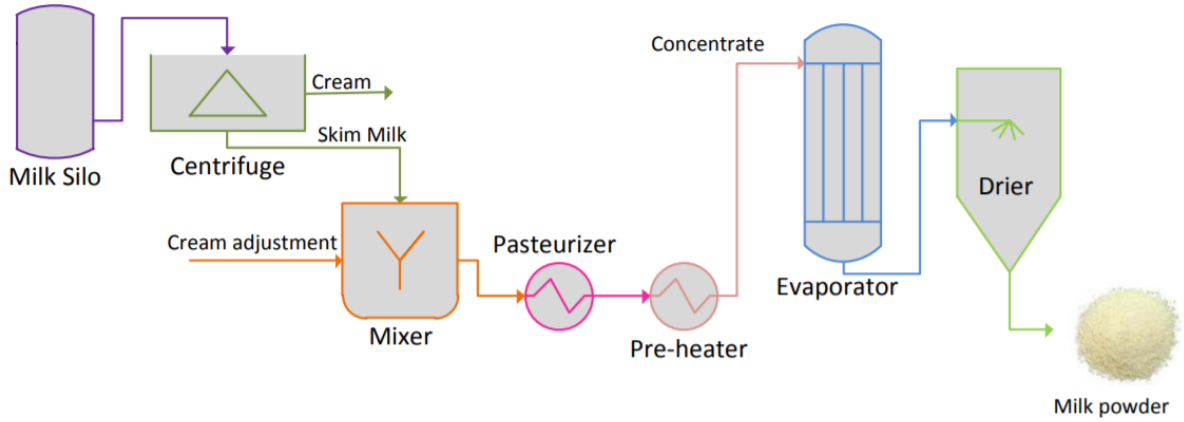

Figure 1.2: Milk powder process beginning to end [4]

This research is focused on the evaporator. A falling film evaporator is a large vertically-placed vessel whereby the inside is filled with smaller tubes. Steam enters the vessel and heats up the outside of the smaller tubes. Milk is flowing through the inside of the smaller tubes. Water is separated from the milk by evaporation. The quality of the milk must be preserved during the heating.
Having a closer look at the milk side, it appears that the tube is not completely filled with milk. Milk is flowing *only* along the inside perimeter. The advantage of this process is that a thin layer of liquid is continuously in contact with the wall. The flow is called a falling film if the thickness comparing to the length of the flow is very small. The wall is heated with steam from the outside, the water in the milk will evaporate. A total overview of an evaporator is given in figure 1.3. The milk comes in from the top (A), and the product leaves at the bottom (B). Steam enters the evaporator at the top

(D) and leaves where the tubes ends (C). Inside the tubes, vapour is formed as well. This vapour is separated from the milk in the calandria base. The vapour flows via the separator duct into the separator. In the separator, the last residues of milk are leaving at the bottom (B) and the vapour flows out of the separator on the top (E).

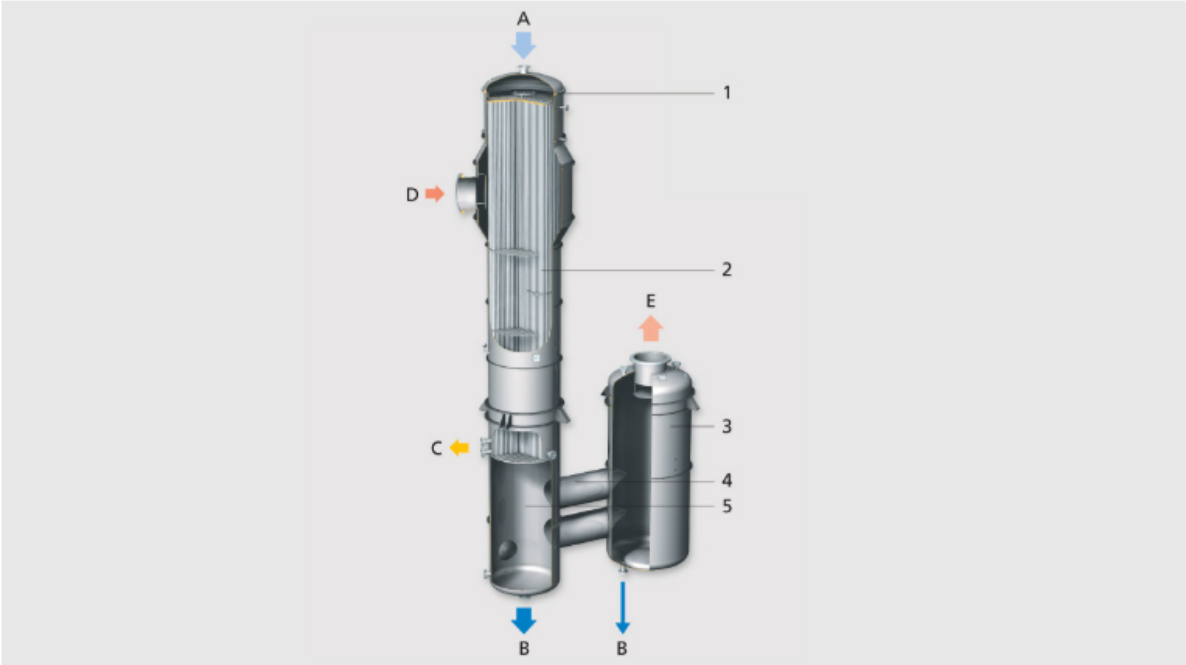

A = Product, B = Concentrate, C = Condensate, D = Heating steam, E = vapor, 1 = Head, 2 = Calandria, 3 = Separator, 4 = Separator duct, 5 = Calandria base

Figure 1.3: Falling film evaporator [5]

The head section of the falling film evaporator has plates which divide the milk equally over the small tubes (fig. 1.4). With the holes made in the distributor, the milk falls in the middle of the plates of the tubes. From the middle the milk is distributed equally to each tube and creates a falling film.

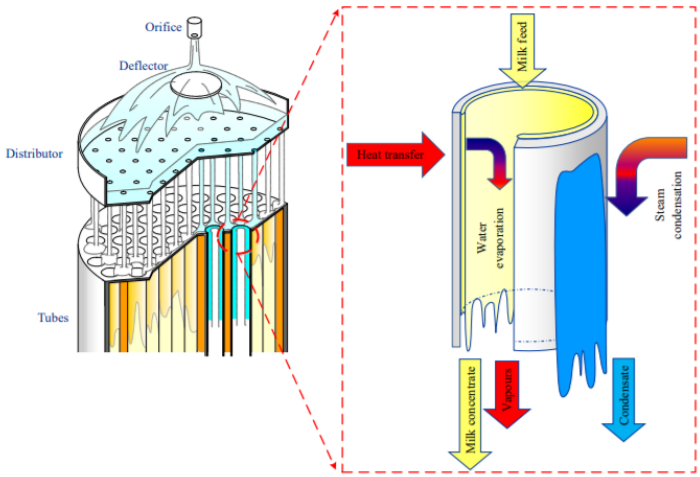

Figure 1.4: Evaporator working principle [4]

To visualize the flow, experiments have been performed by Gourdon et al., where milk flows at the outside of the tube [6]. This is opposite for this research, it only gives an example of the film layer. Figure 1.5, produced by Gourdon et al., shows two examples of a falling film for two distinct distances from the inlet. The left figure shows a falling film at the beginning of the evaporator, while the right figure shows a more viscous film, which is further into the evaporator.

(a) 0,3 m from inlet (b) 4 m from inlet

Figure 1.5: Falling film flow of approximately 50 percent solid at different heights in the evaporator [6]

1.2. Falling film evaporator

In the past decades several researchers have studied the falling film evaporators to understand the relevant heat transfer mechanisms. Starting in 1990, Winchester and March [7] noticed that falling film evaporators are widely used but not well understood. An energy balance has been proposed as goal to make a dynamic and controlling system of the falling film evaporator. The assumption was that the film velocity, liquid density, latent heat and the heat transfer coefficient are constant. The breaking of the film due to surface tension can be avoided by using multiple stages. They also suggested that a film exist of two layers; laminar layer close to the wall and a turbulent layer by the moving vapour.

Processing milk consumes around 300 to 500 GWh per million metric tons. Heating and steam generation is responsible for 60 to 75 percent of the energy used. The energy is intended for the falling film evaporator and the drying afterwards [8]. In the paper of Ruan et al. [9], a mass, energy, phase equilibrium and heat transfer rate equation are captured in a matrix model. Their research focuses on the energy saving of a triple effect evaporation system. To do so, the system is combined with a heat pump, condensed water flash and solution flash which gives a saving of about 28 percent. For the heat transfer coefficient an empirical correlation is used.

The research of Zhang et al. compared the different kinds of falling film evaporators, namely the conventional five-effect evaporator and the three-effect evaporator with mechanical vapour recompression (MVR) are compared. An effect is a body of an evaporator. The MVR consumes only one-third of the energy compared to the conventional evaporator. The research has been done under vacuum, because it minimizes the adverse impact of heat on the thermal sensitivity milk components. The simulation was performed in a commercial package, comprehensive thermodynamic package and advanced computation methods. The overall heat transfer is selected as a fixed value of 2200 $W\,m^{-2}\,K^{-1}$ [10].

The residence time in a falling film evaporator, which is the required time to go completely through the chosen section, depends on the state of the falling film. When the film is in a wavy laminar regime, less time is needed than by a laminar regime. This is concluded, based on an experimental data from the setup of Silveira et al. In figure 1.6 the horizontal axis is the residential time and the vertical axis is the residence time distribution [11].

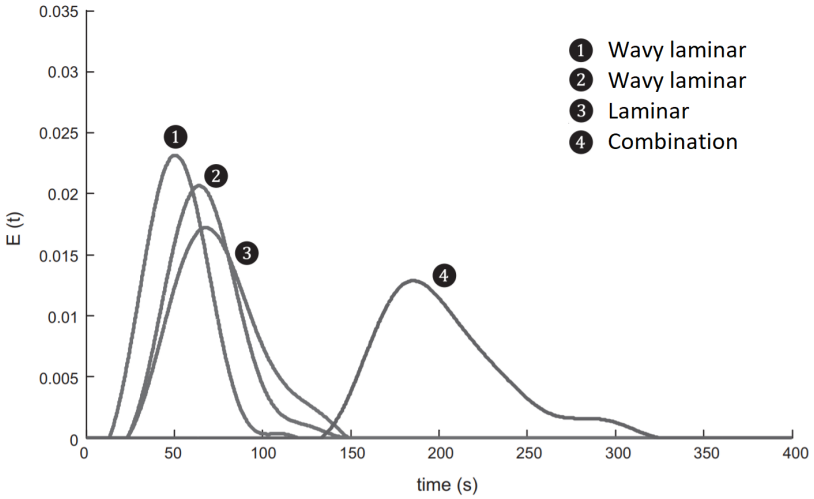

Figure 1.6: Residence time in the falling film evaporator. [11]

The vapour flow inside the tube has influence on the behaviour of the falling film. When the vapour flow has a higher velocity then the falling film layer, it makes the falling film more turbulent which results in a higher heat transfer coefficient. However, when the vapour flow is too fast, tears will be formed and will detached from the wall. In the paper of Chun et al. there is an eddy-viscosity distribution function proposed to predict the thickness and heat transfer of a turbulent falling film of water:

$$\frac{E_m}{\nu} = -1/2 + 1/2 \left[1 + 4\, K^2\, y^{+2} \left(1 - \frac{s^3\, y^+}{\delta^+} \right)^2 D^2 \right]^{1/2} \tag{1.1}$$

with K the Von Kármán's constant, y the distance measured from the wall, δ the film thickness, D the van Driest damping coefficient and s is a combined factor with density, gravity, film thickness and shear stress. Some of these parameters are hard to predict. But when the prediction is made correct, the experimental data is in good agreement for a wide range of film Reynolds number and dimensionless shear stress [12].

Research on the tube has been done by Wei Li et al. [13] for water. The paper draws several conclusions. Increasing the inlet temperature will lead to an increase of the overall heat transfer coefficient. Furthermore, when the pipe has a pattern inside, so instead of a smooth pipe, the overall heat transfer increases as well. The correlation used for predicting have an error of less than 30 percent.

The fouling factor is a factor which has to be taken into account when investigating the falling film evaporators. The fouling has impact on cleaning, energy and operation costs. It is important to keep the tubes wet to avoid fouling, so that poor liquid distribution and falling film break up can be avoid. Fouling has also the property to have a non-uniform formation along the tube. Furthermore, fouling is a complex phenomenon which involves the denaturalization of the protein β - lactoglobulin by thermal treatment. It has effects on several factors, such as product composition, temperature, PH and geometrical aspects [14].

In June 2017, research was performed by Cyklis for a falling film juice evaporator to investigate the theoretical heat transfer coefficient [15]. However, juice has slightly different properties than milk. To validate the theoretical model, an experimental setup has been built. Multiple parameters are varied in this setup. The diagrams are made for a five-effect falling film evaporator, where the feed

is 20 t/h. The outer diameter of the tube is 38 mm with a tube wall thickness of 1.5 mm, total amount of tubes is 163, length is 9.5 m and the total area of 178 m^2. In the theoretical part, three methods are opposed to each other. The first method is proposed by Verein Deutscher Ingenieure (VDI), the second and third methods are proposed by papers, Prost et al. (PGU) and Chun & Seban (CS). In figure 1.7a the results of the convection of the falling film are presented.

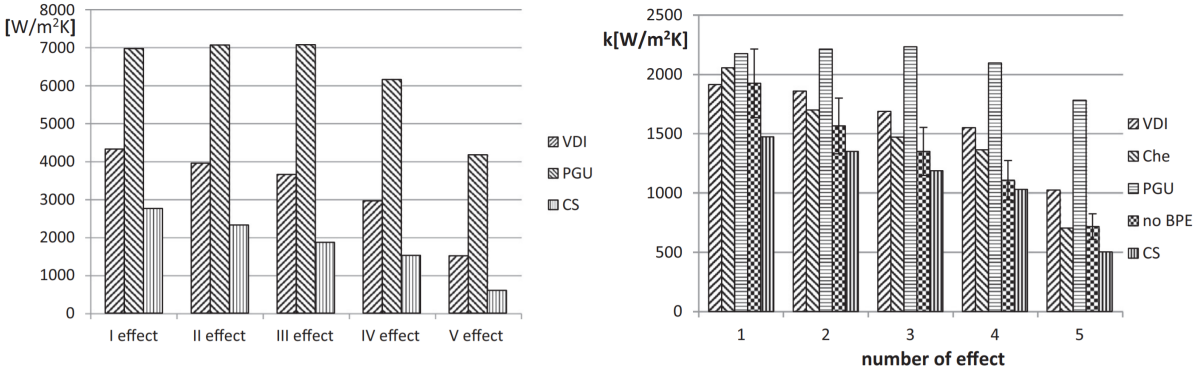

(a) (b)

Figure 1.7: (a) Heat transfer by convection and (b) overall heat transfer coefficient

In figure 1.7b two extra methods have been added, first one is based on a website (Che). The second added method (no BPE) is the experiment which has been performed. The paper is not showing which method has been used for determining the overall heat transfer coefficient. It has been concluded that the VDI, CS and CHE method can be used for calculating the overall heat transfer coefficient.

Nucleation can occur when the temperature difference in the falling film increases. This usually happens at a difference of more than 7 °C between the wall temperature and the boiling temperature of the fluid. Nucleation is undesired for the process because of the risk of fouling. In figure 1.8 is the horizontal axis gives as the heating rate in $\dot{q}$, W m^{-2}, and the vertical axis as the heat transfer coefficient in α, W m^{-2} K^{-1} [16].

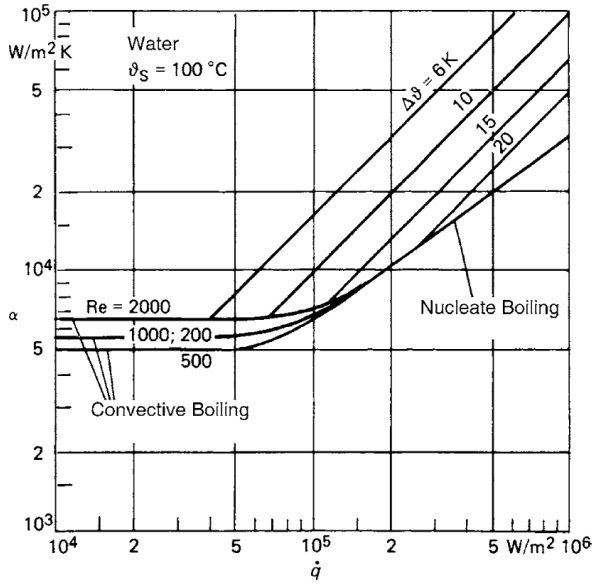

Figure 1.8: Regime of convection and nucleated boiling [16].

In the paper of Numrich [19], the turbulent falling film is divided into three sections, valid up to Prandtl number of 50. Figure 1.9 indicates the wall of the tube, the three sections and the surface of the falling film. Section 1 is close to the wall and has a laminar profile. The middle section is the core section with a turbulent profile and the third section is the interface area between the falling film and the vapour phase.

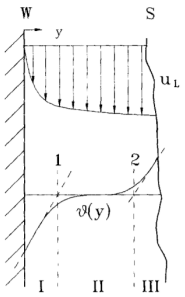

Figure 1.9: Sections in a turbulent falling film [19].

In figure 1.10 results are shown, which has been done in 1990 by Jebson et al. On the horizontal axis, the effect number is ordered differently, it follows the liquid flow pattern. On the vertical axis is the overall heat transfer coefficient. It can be observed that the fluctuation is significant. For the heat flux, the total energy is taken, divided by the total area. The reason for fluctuation is the large number of different factors playing a role. There are design factors, such as viscosity, vapour momentum and temperature difference. Also operating factors like, liquid distribution, fouling inside and outside tubes, calandria angle, gas blocking and restricted condensate flow which causes fluctuation [20, 21]. The calandria is the body of the falling film evaporator.

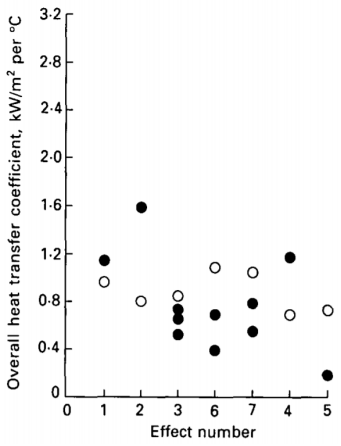

Figure 1.10: Seven-effect evaporator of concentrating whole milk, the open circle is test 1, the filled circle is test 2 [20]

A pilot plant has been built by Silveira et al. to investigate the effectiveness of evaporation of skim milk [22]. The pilot plant consists of three tubes with a diameter of respectively 36 mm, 23 mm and 23 mm. The tubes are heated individually by an electrical heating system. The total power of the heating is 25.2 ± 0.05 kW. The pressure in the tube is maintained at 0.02 MPa, so the evaporation temperature is maintained at 60 °C. The temperature difference is higher than 10 °C. The mass flow rate is 50 ± 0.7 kg/h. For the overall heat transfer coefficient, the value is between 1.24 W/m² °C and 1.96 W/m² °C.

1.3. Research outline

From literature review on falling films follows that the overall heat transfer coefficient is not well understood yet. Most researchers use a constant value in their model. Halfway 2017, the first comparison between theoretical knowledge and experimental observation has been done for a falling juice evaporator. A better estimation of the overall heat transfer coefficient leads to a better understanding of the falling film evaporator and to an optimized thickness of the falling film. The efficiency increases by optimizing the thickness as the energy usage is reduced. Therefore, the main research question in this research is formulated as:

" The objective of this research is to determine theoretically the local overall heat transfer coefficient of the falling film and to investigate experimentally the applicability of heat flux sensors by determining the local overall heat transfer coefficient. "

The reason for investigating the overall heat transfer coefficient with heat flux sensors is given by the restriction of a falling film. Once a falling film is disturbed, the falling film will proceed at a different path. The heat flux sensors allow for local non-intrusive measurements. The advantage of knowing the local overall heat transfer coefficient is that it can predict the thickness of the liquid at the inside of the tube. So, for the running operation, it will detect any dry spots.

The approach to determine the applicability of the heat flux sensors is performed by building an experimental setup. However, the heat flux sensors which will be applied on the falling film evaporator are not determined yet. To do so, a theoretical analysis is made for the falling film evaporator where the heat flux is calculated. The heat flux is needed for the selection of the heat flux sensor. In the experimental setup, the tube is completely filled with water. This is well-known and described in literature. The results and accuracy of the experimental setup can be compared with the theoretical local overall heat transfer coefficient of the falling film evaporator. So, it can be determined if the heat flux sensors are applicable to use on the falling film evaporator.

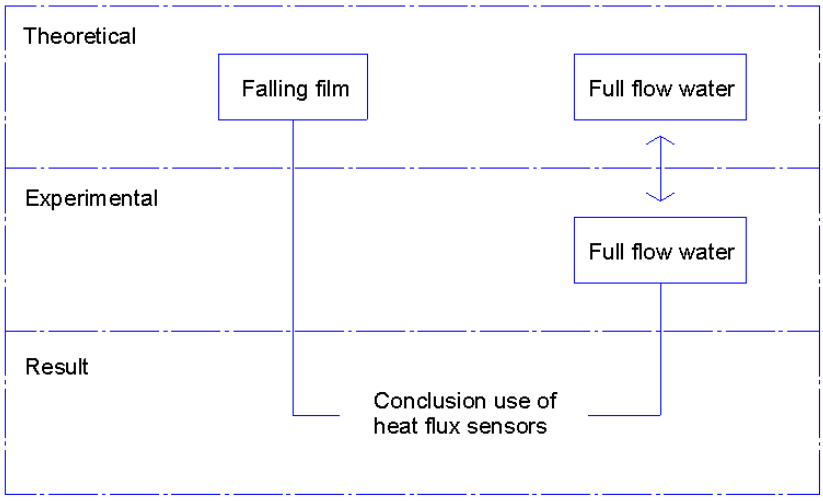

Figure 1.11: Overview of research design

2

Theory

In the first section, the principles of heat transfer are discussed. These principles provide a framework for the overall heat transfer coefficient. The second section explains the behaviour of the falling film in a mathematical framework. The last section investigates a full flow water in a tube, which will be used to test the heat flux sensors.

2.1. Principle of heat transfer

To know the amount of heat flowing from the steam into the tube containing milk, the heat transfer must be investigated. Heat is defined as: "energy transfer due to temperature gradients or differences" [23]. There are three different types of heat transfer, namely conduction, convection and radiation. The radiation is less important in this research. To theoretically estimate the total heat transfer through an object, all the heat transfer should be taken into account. This combination is known as the overall heat transfer coefficient.

The conduction of heat through an object is described by Fourier law. His work states that heat always tends to an equilibrium. This process can be described by the following mathematical equation which comes out of experimental work [24].

$$\dot{Q} = -A\,k\,\frac{dT}{dx} \tag{2.1}$$

where $\dot{Q}$ is the rate of heat transfer, A is the area, k is the thermal conductivity, T is the temperature and the distance is given by x. In words, the heat through an object depends on the temperature difference, distance, area and the thermal conductivity of the material.

Transport of energy by bulk motion of a medium is called convection [23]. Mostly applied from surface to a moving fluid. The surface can be in any geometry and temperature difference, which makes the convection complicated. Furthermore, the heat transfer rate is higher at a turbulent flow than at a laminar flow. The general, linear characteristic equation used for convection is:

$$\dot{Q} = -A\,h_c\,\Delta T \tag{2.2}$$

$$\Delta T = T - T_\infty \tag{2.3}$$

where h_c is the convection term. This equation is also known as Newton's law of cooling [23, 25, 26].

To include all the modes of heat transfer, an overall heat transfer coefficient is determined. The overall heat transfer coefficient compose the modes by the use of electrical analogy. An electrical analogy has the purpose to take all the resistances together and give one combined value. So a general steady state, quasi one-dimensional overall heat transfer coefficient has the following equation and in figure 2.1 is the electrical analogy drawn.

$$\frac{1}{U} = \frac{1}{h_{c,i}} + \frac{L}{k} + \frac{1}{h_{c,o} + h_{r,o}} \tag{2.4}$$

where the U is the overall heat transfer coefficient, h_c is the convection, L is the thickness of the wall, k is the thermal conductivity and the h_r is the radiation.

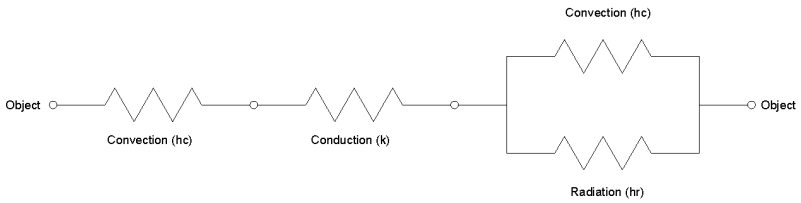

Figure 2.1: General electrical analogy

2.2. Falling film

The falling film is a thin layer of liquid streaming along a vertical surface. The falling film is influenced by the shear stress induced by the wall and gravity. By investigating the falling film, it appears that it has three different regimes. The first regime is at very low Reynolds number for which the surface of the falling film is smooth. This regime is known as the laminar falling film. Ripples start to appear when the Reynolds number increases. This is the second regime and called the wavy laminar falling film. The last regime is visibly influenced by gravity and is known as turbulent falling film.
There the regimes depend on Reynolds number, the final Reynolds number of a falling film is given in equation 2.8. Starting with the general definition of Reynolds number:

$$\text{Reynolds number} = \left\{ \frac{\text{Inertial forces}}{\text{Viscous forces}} \right\} = \frac{\rho_{\text{milk}}\, u_{\text{milk}}\, D_h}{\mu_{\text{milk}}} \tag{2.5}$$

For a falling film, the velocity and the hydraulic diameter in a falling film are defined as:

$$u_{\text{milk}} = \frac{\Gamma}{\rho_{\text{milk}}\, \delta} \tag{2.6}$$

$$D_h = \frac{4\, A_c}{P} = 4\, \delta \tag{2.7}$$

Combining equation 2.5 with equation 2.6 and 2.7 gives:

$$Re_{milk} = \frac{4\, \Gamma_{\text{milk}}}{\mu_{\text{milk}}} \tag{2.8}$$

where ρ is the density, Γ the mass flow rate per unit width, A_c the cross-section area, P_m the wetted perimeter and δ is the thickness of the film.

Figure 2.2a is a schematic overview of a falling film which is heated from the tube wall. The thickness of the falling film starts to decrease over distance. The circle is a close up, indicated by figure 2.2b. It is visible that there are waves present in the falling film, which means that the falling film is in a transition or turbulent regime [27].

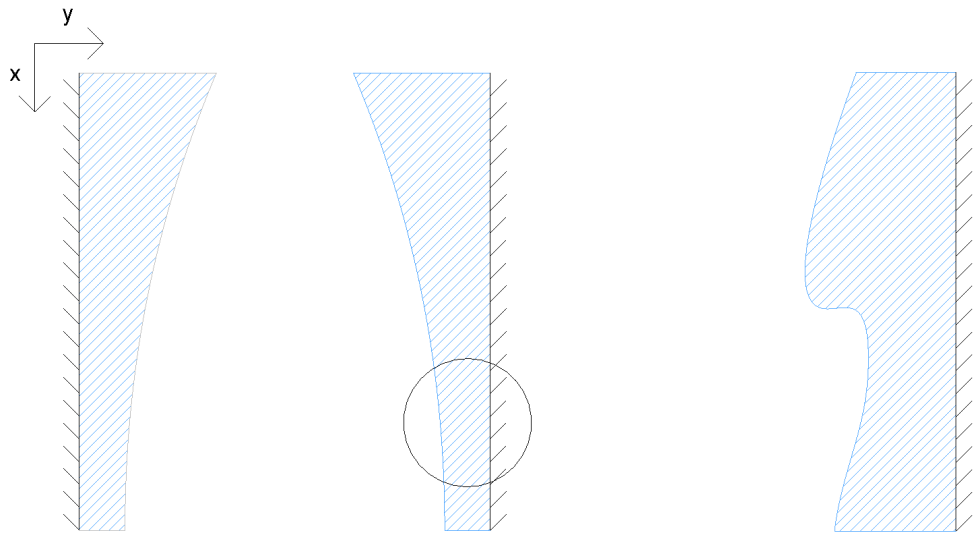

Figure 2.2: (a) Schematical evaporation falling film and (b) close up falling film at wavy laminar or turbulent regime

2.3. Heat transfer in falling film

As discussed earlier, the first regime of the falling film is the laminar falling film. This regime is calculated by using the theory. First the dynamics of the fluid is taken into account, after that the heat transfer. The fluid dynamics can be subdivided into the mass conservation and momentum conservation. The heat transfer can be subdivided as well into the local convection and energy conservation. Solving the different subdivision will give the relation between the Nusselt number and the Reynolds number. This equation is used for the calculation of the falling film of milk. Parts of this section are based on the book of Basic Heat and Mass Transfer written by Mills [23].

2.3.1. Fluid dynamics

Taking a volume element in the falling film, with a small length and width which is constant at the same place, mass changes can be investigated. The change of mass is obtained by determining the thickness of the falling film. The amount of mass going in the system is equal to the amount of mass leaving the system minus the mass which leaves the system by evaporation, so:

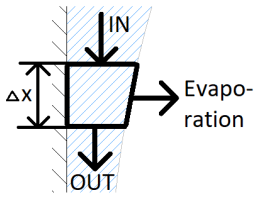

Figure 2.3: Element volume for mass balance

$$\int_0^{\delta(x)} \rho_l \, u dy|_x = \int_0^{\delta(x)} \rho_l \, u dy|_{x+\Delta x} + \dot{m}'' \, \Delta x \tag{2.9}$$

where $\dot{m}''$ is the evaporation rate per [kg m^{-2} s^{-1}].

When Δx goes to zero:

$$\dot{m}'' = -\frac{d}{dx} \int_0^{\delta(x)} \rho_l \, u dy \tag{2.10}$$

The behaviour of the flow has a large influence on the heat transfer coefficient. Using the Navier-Stokes equation, the velocity and the amount of mass per unit width (Γ) of the falling film can be determined for a laminar condition:

$$\rho\left(\frac{\partial u}{\partial t}+u\frac{\partial u}{\partial x}+v\frac{\partial u}{\partial y}+w\frac{\partial u}{\partial w}\right)=-\frac{\partial P_{\infty}}{\partial x}+\mu\left(\frac{\partial^2 u}{\partial x^2}+\frac{\partial^2 u}{\partial y^2}+\frac{\partial^2 u}{\partial z^2}\right)+\rho\ g \tag{2.11}$$

Taking a detail look at the Navier-Stokes equation, a few things can be simplified. The falling film can be seen as a two-dimensional object for now, so the three-dimensional component can be taken out of the equation. Meaning that w and z terms drops out of the equation. Furthermore, it is assumed that the flow is in steady state, so the time dependent factor drops out as well. The temperature of the vapour inside the tube is equal to the saturation temperature and it is assumed that the velocity of the vapour is zero.
The simplified Navier-Stokes equation can be non-dimensionalized. Starting with the non-dimensionalizing of the continuity equation (eq. 2.12) to obtain the scaled velocity.

$$\frac{\partial u}{\partial x}+\frac{\partial v}{\partial y}=0 \tag{2.12}$$

It is assumed that the $\delta \ll L$ so the non-dimensional variables give for the Navier-Stokes equation that $\frac{\partial^2 u}{\partial x^2} \ll \frac{\partial^2 u}{\partial y^2}$. Furthermore, the term on the left side of the equation (eq. 2.11) is very small in comparison with $\frac{\partial^2 u}{\partial y^2}$, so it can be neglected. Remaining:

$$\mu\left(\frac{\partial u^2}{\partial y^2}\right)+\rho_l\ g=0 \tag{2.13}$$

Integrating the equation (eq. 2.13) using boundary conditions. The first boundary condition is at the wall, where the velocity is zero because of the no-slip condition. The second boundary condition is at the edge where fluid is in contact with the vapour. For the second boundary condition, the shear stress between the interface of the liquid and vapour is zero. The y-axis is set out on horizontal direction, see figure 2.2a. After integration, the mass flow rate per unit width, Γ, and the velocity profile are calculated.

$$\Gamma=\int_0^{\delta}\rho_l\ u dy=\frac{g\ \delta^3\ \rho_l}{3\ \nu} \tag{2.14}$$

$$u=\frac{\rho_l\ g\ \delta^2}{\mu_l}\left[\frac{y}{\delta}-\frac{1}{2}\left(\frac{y}{\delta}\right)^2\right] \tag{2.15}$$

Combining equation 2.8 and equation 2.14, the Reynolds number becomes:

$$\frac{\delta}{(\nu^2/g)^{\frac{1}{3}}}=\left(\frac{3}{4}Re\right)^{\frac{1}{3}} \tag{2.16}$$

where $(\nu^2/g)^{\frac{1}{3}}$ has the dimension of length.

At a wavy laminar and turbulent regime, the velocity varies at each position because liquid builds up and waves can be formed on the surface of the falling film. This has effect on the velocity of the falling film. When the wave has passed, the velocity will decrease. The equation used is:

$$u=Re\ \frac{\mu}{4\ \delta\ \rho} \tag{2.17}$$

2.3.2. Heat transfer

To find a relation between the Nusselt number and Reynolds number, the local convection and energy conservation must be determined as well.

The heat goes from the tube into the falling film. For the tube is assumed that the temperature distribution is linear. The two boundary conditions are located at the wall, temperature of the tube and at the surface of the film, as the saturation temperature:

$$q = \frac{k_l\,(T_w - T_{sat})}{\delta} = k_l \frac{\partial T}{\partial y}\Big|_w \tag{2.18}$$

The local heat transfer coefficient is:

$$h = \frac{q}{\Delta T} \tag{2.19}$$

Combining both equations gives:

$$h = \frac{k_l \frac{\partial T}{\partial y}\Big|_w}{T_w - T_{sat}} \tag{2.20}$$

The flow is assumed to be steady for this energy equation. Just as with the mass conversation, an element volume approach has been taken.

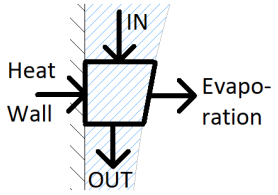

Figure 2.4: Element volume for energy balance

The equation becomes:

$$-\dot{m}''\, h_g\, \Delta x + \int_0^{\delta(x)} \rho_l\, u\, h_l dy|_x = \int_0^{\delta(x)} \rho_l\, u\, h_l dy|_{x+\Delta x} + k_l \frac{\partial T}{\partial y}\Big|_w \Delta x \tag{2.21}$$

Again, let Δx go to zero and rearrange:

$$k_l \frac{\partial T}{\partial y}\Big|_w = -\dot{m}''\, h_g - \frac{d}{dx}\int_0^{\delta} \rho_l\, u\, h_l dy \tag{2.22}$$

Insert the mass equation which is found in equation 2.10. Giving:

$$k_l \frac{\partial T}{\partial y}\Big|_w = \frac{d}{dx}\int_0^{\delta} \rho_l\, u\, (h_g - h_l) dy \tag{2.23}$$

The enthalpy of the liquid is h_l and vapour is h_g. For a constant liquid specific heat capacity:

$$k_l \frac{\partial T}{\partial y}\Big|_w = \frac{d}{dx}\int_0^{\delta} \rho_l\, u[h_{fg} + c_p(T_{sat} - T)] dy \tag{2.24}$$

where the term $c_p(T_{sat} - T)$ is negligible in comparison to the phase change enthalpy. Combining equation 2.14 and equation 2.23, the energy equation becomes:

$$k_l \frac{\partial T}{\partial y}\Big|_w = h_{fg} \frac{d}{dx}\int_0^{\delta(x)} \rho_l\, u\, dy = h_{fg} \frac{d\Gamma}{dx} \tag{2.25}$$

To determine the thickness, the mass per unit width (eq. 2.14), as well as the local heat transfer coefficient (eq. 2.20), are used. Together with equation 2.25 it becomes:

$$\frac{d\Gamma}{dx} = \frac{g\,\rho_l\,\delta^2}{\nu_l}\left(\frac{d\delta}{dx}\right) \tag{2.26}$$

Combining equation 2.26 and equation 2.25 give after integration:

$$\delta = \left[\frac{4\,x\,k_L\,(T_w - T_{sat})\,\nu_l}{h_{fg}\,\rho_l\,g}\right]^{1/4} \tag{2.27}$$

For the wavy laminar and turbulent falling film, the thickness is an empirical equation. As can be seen in figure 2.2b, the thickness varies along the tube. Therefore, a prediction is given by Gourdon et al. for the wavy laminar thickness [28]:

$$\delta = (0.599\,\frac{\nu_l^2}{g}\,Re)^{1/3} \tag{2.28}$$

And the thickness of turbulent falling film is [19]:

$$\delta = 0.288\left(\frac{\nu_l^2}{g}\right)Re^{0.53} \tag{2.29}$$

2.3.3. Relation between the Nusselt number and Reynolds number

To obtain a relation between Nusselt number and the Reynolds number, the general Nusselt number for a falling film is given first:

$$\text{Nusselt number} = \left\{\frac{\text{Convective heat transfer}}{\text{Conductive heat transfer}}\right\} = \frac{h\,(\nu^2/g)^{\frac{1}{3}}}{k_l} \tag{2.30}$$

This relation combines the energy equation 2.25 with equations 2.8, 2.20 and 2.30:

$$\frac{dx}{(\nu^2/g)^{\frac{1}{3}}} = -\frac{\mu_l\,h_{fg}}{4\,k_l\,(T_{sat} - T_w)\,Nu}dRe \tag{2.31}$$

Using Prandtl number and Jakob number:

$$Pr_l = \left\{\frac{\text{Viscous diffusion rate}}{\text{Thermal diffusion rate}}\right\} = \frac{c_{p,l}\,\mu_l}{k_l} \tag{2.32}$$

$$Ja_l = \frac{c_p(T_{sat} - T_w)}{h_{fg}} \tag{2.33}$$

The Jakob number is the ratio of sensible heat to latent heat absorbed (or released) during the phase change process [29].

The equation becomes:

$$\frac{L}{(\nu^2/g)^{\frac{1}{3}}} = -\frac{Pr}{4Ja}\int_{Re_0}^{Re_L}\frac{dRe}{Nu} \tag{2.34}$$

As already mentioned above, there are three regimes in falling films. The first regime is below a Reynolds number of 30. The second regime is between 30 and Re_{tr}. The last regime is above the Re_{tr}:

$$Re_{tr} = 5800\,Pr_l^{-1.06} \tag{2.35}$$

For the last two regimes, the relation between Nusselt and Reynolds is set in a correlation. These correlations are obtained by experimental data from water [30].

$$Nu = \left(\frac{3}{4} Re\right)^{\frac{1}{3}} \qquad \text{Re} < 30 \qquad \text{(laminar)} \tag{2.36}$$

$$Nu = 0.822\ Re^{-0.22} \qquad 30 \leq \text{Re} < \text{Re}_{\text{tr}} \qquad \text{(wavy laminar)} \tag{2.37}$$

$$Nu = 3.8 \cdot 10^{-3}\ Re^{0.4}\ Pr_l^{0.65} \qquad \text{Re}_{\text{tr}} \leq \text{Re} \qquad \text{(tubulent)} \tag{2.38}$$

Filling these relations (eq. 2.36 - eq. 2.38) into equation 2.34 will give the Reynolds number. Now Reynolds number is known, the Nusselt number can be calculated by:

$$\overline{Nu} = \frac{Pr_l}{4Ja} \frac{(\nu_l^2/g)^{1/3}}{L} (Re_o - Re_l) \tag{2.39}$$

From the Nusselt number, the heat transfer coefficient is calculated with equation 2.40.

$$\overline{h} = \frac{\overline{Nu}\ k_l}{(\nu^2/g)^{(1/3)}} \tag{2.40}$$

Since the transition number depends on the Prandtl number, the following plot is made to visualize the transition points. The dotted line gives the laminar regime, for extreme cases. The line with a slope downwards, just above the dotted line, is the wavy laminar regime. The lines positively-sloped represent the turbulent flow.

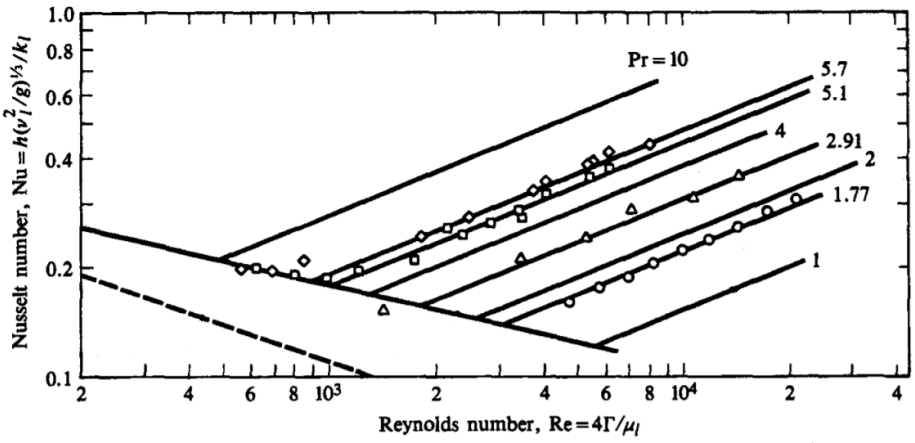

Figure 2.5: Correlation Reynolds number, Nusselt number in falling film [30]

2.3.4. Properties milk in falling film

The medium in the falling film is milk. While the film falls along the inside edge of the tube, the outside is heated with steam. This causes a change in the properties of the milk, because of the evaporation of water from the milk. The mass fraction is taken into account, to take care of the properties of the milk. For the thermal conductivity (k_{milk}), density (ρ_{milk}) and heat capacity ($c_{\text{p,milk}}$), the following equations have been used [28]:

$$k_{milk} = 0.5656 - 0.2692\ S + 0.9122 \cdot 10^{-3}\ T_{sat} - 0.2083\ S^2 + 0.79 \cdot 10^{-3}\ S\ T_{sat} - 0.1417 \cdot 10^{-5}\ T_{sat}^2 \tag{2.41}$$

$$\rho_{milk} = 98.02\ S^2 + 236.3\ S + 978.9 \tag{2.42}$$

$$c_{p,milk} = -2655\ S + 4227 \tag{2.43}$$

where S is the dry solid mass fraction and T_{sat} is the saturation temperature of milk. There the fluid becomes non-Newtonian at a solid dry mass fraction of 0.45, an exponential function is used to cover the range of the dynamic viscosity at saturation temperature [28].

$$\mu_{milk} = 0.0004804\ e^{10.9S} \tag{2.44}$$

2.4. Full flow water

The local overall heat transfer coefficient is determined for a full flow of water. The reason to start with a full flow of water is that the experimental results are better to verify than the falling film, where more parameters can influence the results. When the system is filled with water, there are two different phenomena which should be taken into account. The first phenomena is the friction which occur in the system. The second phenomena is the heating of certain part of the tube.

2.4.1. Pressure loss

The goal of the pressure loss calculation is to determine the characteristics of the pump which will be installed. The assumption which are made to calculate the pressure loss are: fluid in the system is a Newtonian fluid and incompressible. The pressure loss can be calculated by the friction loss.

The head loss is given by:

$$h_f = f\frac{L\ u^2}{d\ 2g} \tag{2.45}$$

where h_f is the head loss, f the non-dimensional friction factor, L the length, d the diameter, u the velocity and g is the gravitational acceleration. Calculating the pressure losses in the system for straight parts, the following equation 2.46 is used:

$$\Delta P = h_f\ \rho\ g \tag{2.46}$$

From the Navier-Stokes equation 2.11, the energy equation can be obtained with the following assumptions; namely steady state, incompressible and inviscid:

$$p_1 + \frac{\rho u_1^2}{2} + \rho\ g\ z_1 = p_2 + \frac{\rho u_2^2}{2} + \rho\ g\ z_2 + h_f \tag{2.47}$$

where z is the height. In a closed system the velocity does not change ($u_1 = u_2$) and the height terms cancel. The pressure loss is caused by the shear stress along the wall. A force balance with pressure loss can be described as equation 2.48. Where the pressure loss times the area is equal to the shear stress along the wall times the length. The sum of these forces is zero.

$$\Delta p\ (\pi\ R^2) - \tau_w\ (2\pi\ R)\ L = 0 \tag{2.48}$$

where R is the radius of the circle, τ_{w} is the shear stress and L is the length of the tube.
Combining equation 2.47 and equation 2.48 gives the head loss related to wall shear stress:

$$h_f = \frac{4\ \tau_w}{\rho\ g}\frac{L}{D} \tag{2.49}$$

Equation 2.49 is applicable for laminar flow.

For a laminar fully developed flow, the shear stress along the wall can be expressed by:

$$\tau_w = \left| \mu \frac{du}{dr} \right| \tag{2.50}$$

where μ is the dynamic viscosity and the velocity profile is given by:

$$u = \left(-\frac{dp}{dx} \right) \frac{R^2}{4\,\mu} \left(1 - \frac{r^2}{R^2} \right) \tag{2.51}$$

For laminar flow, the friction factor can be determined from equation 2.45 and equation 2.49. The friction factor is:

$$f = \frac{8\,\tau_w}{\rho\,u^2} = \frac{64}{Re} \tag{2.52}$$

The laminar flow will be considered until a general accepted threshold of 2300 of the Reynolds number, but depends on the roughness and inlet of the tube. The flow regime becomes turbulent for Reynolds number exceeding the general accepted threshold of 3000. The transition flow is in between. Because turbulent flow is not as straight forward as laminar flow, turbulent flow is based on experimental data. For turbulent flow, the determination of the Darcy friction factor f is done by the equation of Colebrook or Haaland. The equation is based on the Moody diagram which is experimentally determined (figure 2.6). On the horizontal axis stands the Reynolds number and on the vertical axis the friction factor.

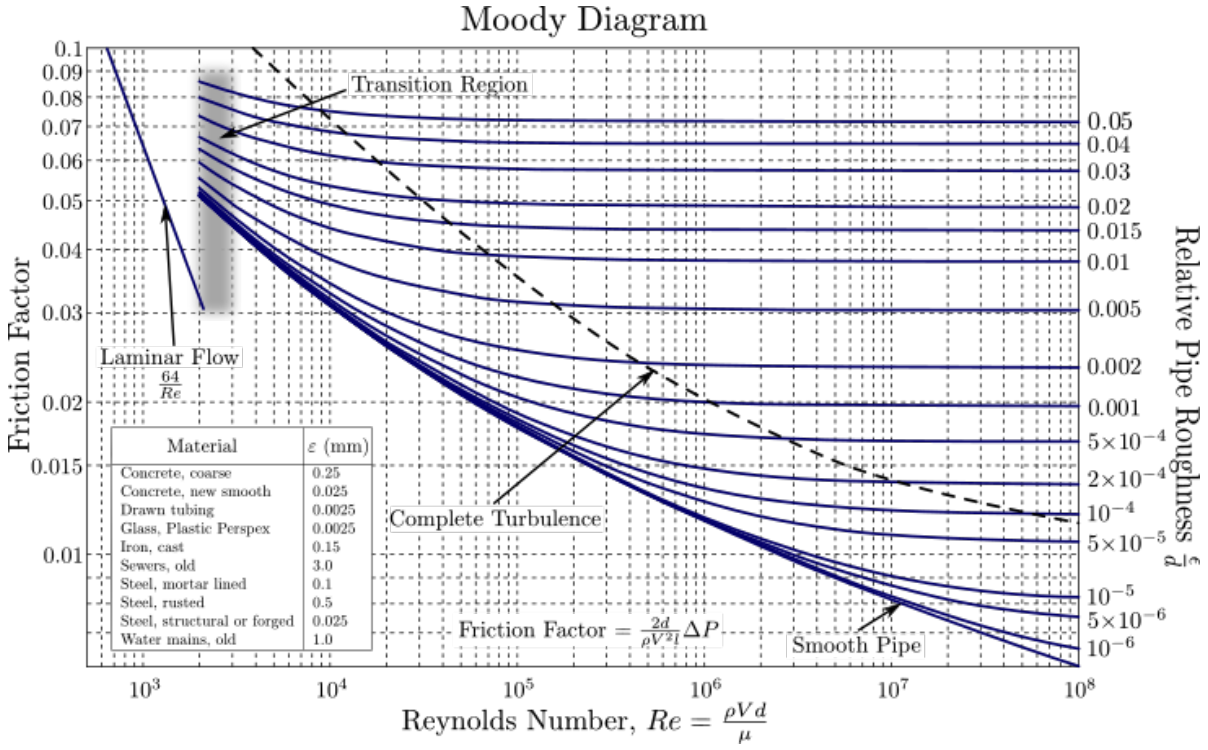

Figure 2.6: Moody diagram [31]

The Moody chart is accurate to ± 15 percent for design calculations over the full range. The Moody diagram is based on the relative roughness of the pipe and the Reynolds number. For the relative roughness of the pipe, the inner wall roughness of the pipe itself has to be known.

$$Haaland: \frac{1}{f^{1/2}} = -1.8\ log\left[\frac{6.9}{Re_D} + \left(\frac{1}{3.7}\ \frac{\epsilon}{D}\right)^{1.11}\right] \tag{2.53}$$

$$Colebrook: \frac{1}{f^{1/2}} = -2\ log\left[\frac{6.9}{Re_D} + \left(\frac{1}{3.7}\ \frac{\epsilon}{D}\right)^{1.11} + \frac{2.51}{Re_D\ f^{1/2}}\right] \tag{2.54}$$

To calculate the pressure loss in obstacles, experimental values are considered [32]. They are expressed as *K*. To determine the pressure loss for *K*, the following equation is used:

$$\Delta h_{f,tot} = \frac{u^2}{2\ g}\left(\frac{f\ L}{D} + \sum K\right) \tag{2.55}$$

Together with the pressure losses of the components, given by the manufactures, the total pressure loss can be calculated.

2.4.2. Thermal phenomena in full flow tube

For a full flow tube, the heat transfer is calculated differently than the falling film. The laminar, transition and turbulent regime can still be defined. A distinguish can be made between the entry of the heated section and the section where the heat transfer is fully developed. A thermal entry length means that the heat must penetrated to the centre of the tube [1]. The thermal heat can be imposed in two different methods. The first method is to give the outside wall of the tube a constant temperature. The second method is by imposing a constant heat flux on the outside of the tube.
The Prandtl number plays a part in the determination of the thermal entry length. Prandtl can be described as follows [23]:

$$Pr = \frac{C_p\ \mu}{k} \tag{2.56}$$

In the research of Sparrow et al. [33] the Reynolds numbers and Prandtl number are varied. The difference between a Prandtl number of 0.7, 10 and 100 is given and it can be seen that the entrance region gets larger when the Prandtl number increases.
To determine the Nusselt number in the laminar entry length, equation 2.57 is mostly used to describe this region. Although it belongs to the constant surface temperature heating, it gives an insight in the parameters influencing the thermal entry length.

$$Nu = 3.66 + \frac{0.065\ \frac{D}{L}\ Re\ Pr}{1 + 0.04[\frac{D}{L}\ Re\ Pr]^{2/3}} \tag{2.57}$$

When L/D goes to infinity, which means further away from the entry, the constant value of 3.66 remains.
The length to came within reach of 5 percent of the fully developed heat profile flow can be determined by the approximation:

$$L = 0.017\ Re\ Pr\ D \tag{2.58}$$

The value of 0.017 originates from the dimensionless Graetz number, which is shown in figure 2.7. Given the length of the thermal entry, the correction on the Nusselt number can be made for the entrance region.

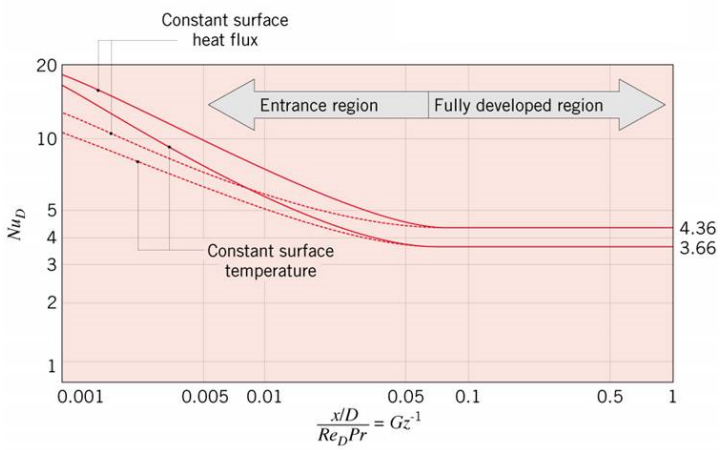

Figure 2.7: Graetz number over Nusselt number

The equation for the constant heat flux is built up from empirical measurements. The equation is completely fitted, see equation 2.59 - 2.61. The correlation has an accuracy within ± 1 percent [34].

$$1.302\left(\frac{x^*}{2}\right)^{-1/3} - 0.5 \qquad 5\cdot 10^{-5} \leq \left(\frac{x^*}{2}\right) \leq 1.5\cdot 10^{-3} \tag{2.59}$$

$$4.364 + 8.68\cdot 10^{3}\left(\frac{x^*}{2}\right)^{-0.506} e^{(-41x^*/2)} \qquad \left(\frac{x^*}{2}\right) > 1.5\cdot 10^{-3} \tag{2.60}$$

$$x^* = \frac{x}{D_h\, Re_{Dh}\, Pr} \tag{2.61}$$

Ndenguma et al. [35] studied the transitional flow experimentally. The medium used is water for three different scenarios: isothermal, heating and cooling. The flow is hydrodynamic and thermally developed where mixed and forced convection can take place. The inlet of the tube is changing. The most useful case for this report is the long calming section. The measurement is done with 9 stations with each two thermocouples embedded in the wall. So, one thermocouple on the top, and the other one at the bottom. The thermocouples are soldered in a groove so that the tube remains in a smooth condition. In figure 2.8 the Reynolds number and the Nusselt number are plotted on respectively the horizontal and vertical axis. The turbulent regime and laminar regime have been investigated thoroughly, but the transitional regime is not supported by a well-known correlation and is plotted using experimental data.

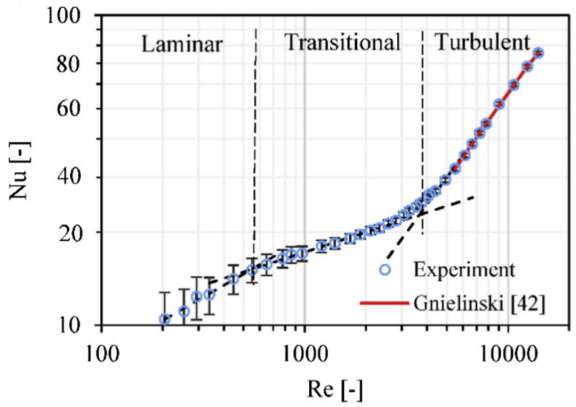

Figure 2.8: Reynolds number over Nusselt number in different regimes [35].

Hasan [36] compared the different correlation of heat transfer at a turbulent region with numerical calculation using finite difference numerical technique. The paper stated that the simulation is successfully compared with experimental work. In the paper of Mills [37], the thermal entry length of a turbulent flow has been discussed. The given definition for the thermal entry length is: "the thermal entrance length is determined by the distance required for Nu_x / Nu_∞ to reach unity". The paper mostly consists of experimental work. The setup uses air as medium, fully developed conditions and a uniform heat flux against the wall. The setup itself has a heated length of 133.5 inch and a 1.5 inch inner diameter. The air has been sucked through the setup. The heating system is a winding of nickel-chromium, with a resistance of 0.37 ohm/ft. The pitch for the wire is 3/8 inch, and the thermocouple is placed in between the wires. Figure 2.9 shows the ratio of the Nusselt number is on the vertical axis. Nu_x is the place of measuring, and Nu_∞ is the area where the Nusselt number becomes constant, which is far away from the entry length. On the horizontal axis, the length is given in the dimension of the distance divided by the diameter of the tube. This has been done so that is can be applied by most tubes.

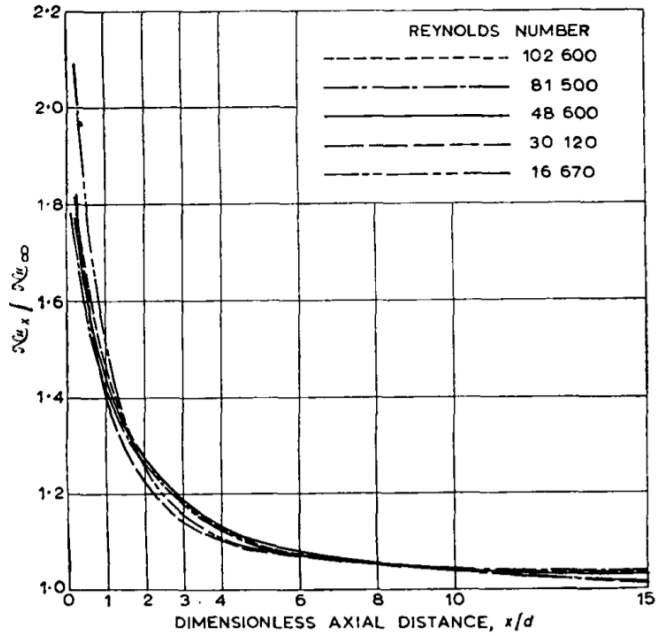

Figure 2.9: Ratio of Nusselt number over the length by a long calming section [37].

The Nusselt number in the turbulence entry region is calculated by the equation of Nusselt [36]. The flow is constrained in between 10 and 400 length over diameter.

$$Nu = 0.036\, Re^{0.8}\, Pr^{1/3} \left(\frac{L}{D}\right)^{-0.055} \tag{2.62}$$

This empirical correlation for a thermal fully developed flow is given by McAdams in 1954 [38]. The range of the experiment is between 10000 and 120000 Reynolds where the Prandtl number is in the range of 0.7 and 120. The data have a deviation of 20 percent. The work has been performed with a constant heat flux at the wall.

$$Nu_{\text{inf}} = 0.023\, Re^{0.8} Pr^{0.4} \tag{2.63}$$

To improve the accuracy, Gnielinski recommended the following equation which is generally used nowadays:

$$Nu_D = \frac{\left(\frac{f}{8}\right)(Re_D - 1000)Pr}{1 + 12.7\left(\frac{f}{8}\right)^{1/2}(Pr^{2/3} - 1)} \qquad (3000 < Re_D < 10^6) \tag{2.64}$$

The range for this equation is bounded by Reynolds. A Reynolds number of 3000 is set as value where in general the flow is fully turbulent.

2.4.3. Heat transfer full flow water

To calculate the local overall heat transfer coefficient, the separated thermal resistances are discussed first. Starting with the water inside the tube. A total overview of the system is given in figure 2.10.

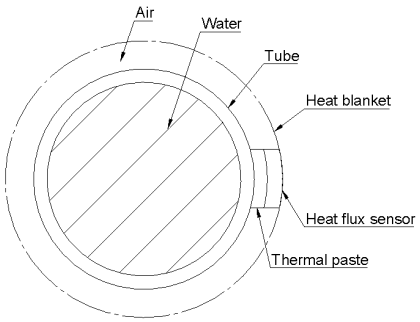

Figure 2.10: Schematic overview tube with components

At low flow rates, the water inside the tube is laminar. For the laminar flow, the Nusselt number is:

$$Nu = \frac{48}{11} \tag{2.65}$$

This constant value of the Nusselt number is based on the assumption of thermal fully developed flow with a uniform wall heat flux. The next step is to apply the first law of thermodynamics with the assumptions of constant fluid properties, low speed flow and negligible change in potential energy. Two boundary conditions are applied. The first boundary condition is at the wall surface where the temperature is equal to the wall surface. The second boundary condition is in the middle of the tube where the derivative over the temperature is zero.
The equation of Gnielinski (eq. 2.64) is applied for turbulent flows. In this equation, Prandtl and Reynolds number are used. Both heavily depend on the temperature due to the fluid properties which are used. At higher power input, the difference between wall temperature and bulk temperature is significant at low flow rates. Two methods are proposed to provide the correct Nusselt number. The first method determines the reference temperature of the fluid.

$$T_r = T_s - \xi\,(T_s - T_b) \tag{2.66}$$

where T_r is the reference temperature, T_s the surface temperature of wall, T_b the bulk temperature and ξ is a constant set a commonly used value of 0.5. For the entry length this correction is not taken into account. The bulk temperature is chosen for the entry length, because the heated layer is still thin and heat is penetrating into the water (fig. 2.11). The line with arrows presents the heat profile of the tube.

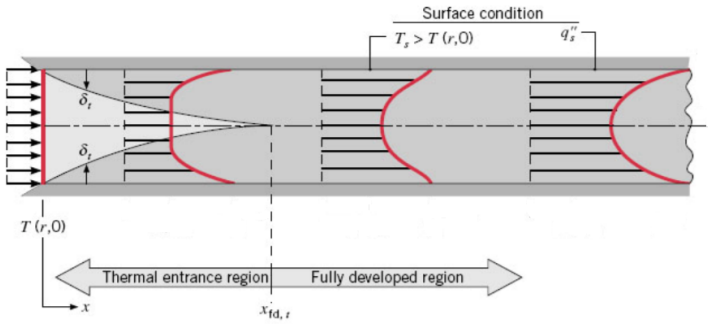

Figure 2.11: Thermal developing flow

The second method takes a correction for the friction factor and the Nusselt number. This correction is based on the kinematic viscosity, due to the large change by a slight temperature difference. The friction factor has influence along the wall. A lower viscosity means less friction.

$$\frac{f}{f_b} = \left(\frac{\mu_s}{\mu_b}\right)^{0.25} \tag{2.67}$$

$$\frac{Nu}{Nu_b} = \left(\frac{\mu_s}{\mu_b}\right)^{-0.11} \tag{2.68}$$

where f is the friction factor and f_b is the friction factor at bulk temperature, μ_s is the kinematic viscosity of the surface and μ_b is the kinematic viscosity of the bulk. The same applies to the Nusselt number relation.

The resistance of the tube, made out of stainless steel, thermal paste and heat flux sensor is conduction, so equation 2.1 is used. Depending on the source, heat blanket or heat flux sensor, the resistance is respectively the full sensor or the half of the heat flux sensor because the temperature and heat flux are measured in the middle of the heat flux sensor. For the heat blanket, the small gap in between the tube and blanket must be included as well. In total, the electrical analogy is:

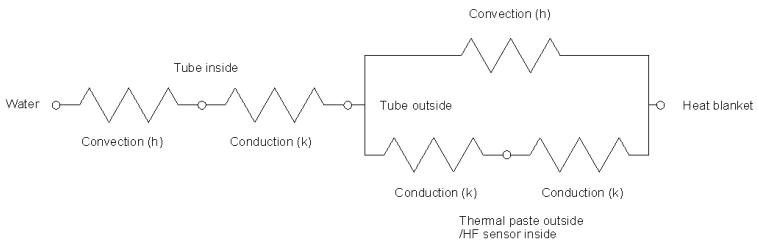

Figure 2.12: Electrical analogy tube

3

Experimental setup

The method for measuring the heat transfer coefficient is discussed in this chapter. An experimental setup is constructed to perform two different experiments. The first experiment is to investigate the local overall heat transfer coefficient for a full flow of water in the tube. The second experiment is the same experiment, only with a falling film instead of the full flow of water. The setup was designed for both experiments. The falling film experiment has not been performed in this research due to time restriction of the project.

3.1. Components in experimental setup

To have a complete overview of the setup, a P&ID is made (fig. 3.1). A P&ID is a schematic illustration of a functional relationship between piping, instrumentation and system components. The P&ID is based on the ISA (Instrumentation, Systems, and Automation Society) directives.

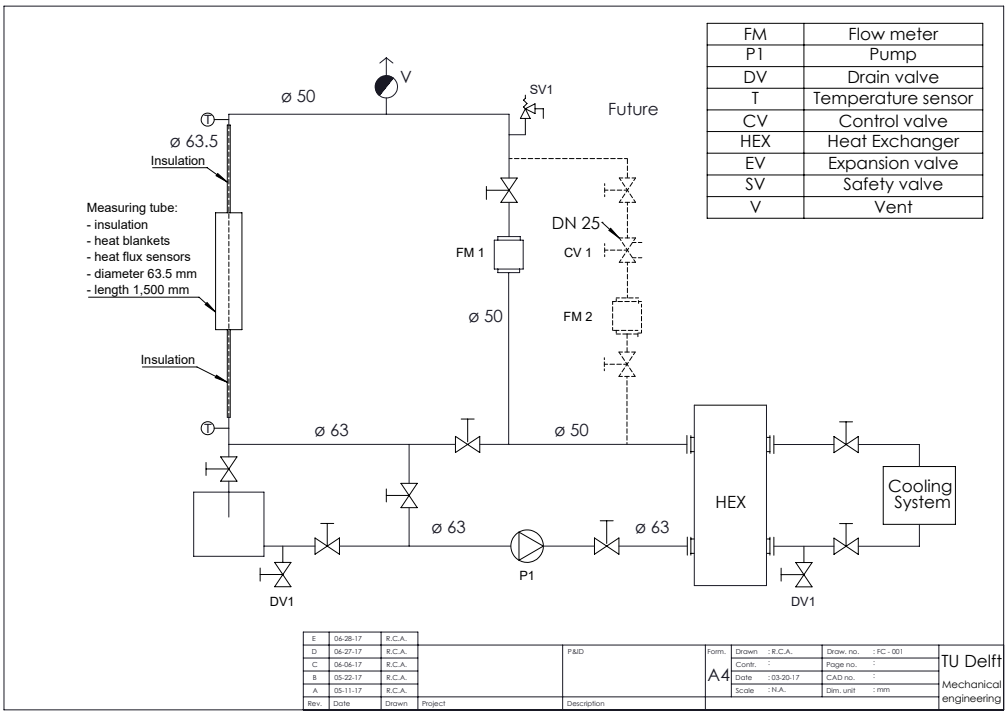

Figure 3.1: P&ID of the setup

The components used in the setup are listed in the P&ID. In the measuring tube on the left side in the P&ID, the measurements are performed concerning the local overall heat transfer coefficient. The tube is made out of stainless steel 304, this is a requirement. From that point, the water can either go into a storage tank or straight to the pump when the valve is closed. The storage tank has a function when the falling film has to be created. It is preferred to have an open system which can be realised with the storage tank. From the pump (P1) the water is transported to a heat exchanger to release the heat. The amount of flow is small when the falling film has to be created. The dotted line is suited for smaller flow rates as in the falling film experiment. For the system fully filled with water, it goes through the flow meter, passes a couple of safety precautions and flows back into the measurement tube.

3.1.1. Selection of cooling system

Before the system was designed, the method of cooling was taken into consideration. There are two possibilities to cool the heated system. The first possibility is the use of a vessel filled with water. This vessel can be used for the open system as well for the closed system. When the closed system is used, the piping should be connected all the way but the water is still cooling the tubes running through the water. Normally, in water which stands still, free or natural convection is directly taken into account. This can also be checked by the following statements for Prandtl > 1:

$$\text{Forced convection} \qquad \frac{Gr}{Pr^{1/3}Re^2} \ll 1 \tag{3.1}$$

$$\text{Mixed convection} \qquad \frac{Gr}{Pr^{1/3}Re^2} \approx 1 \tag{3.2}$$

$$\text{Natural convection} \qquad \frac{Gr}{Pr^{1/3}Re^2} \gg 1 \tag{3.3}$$

where the Grashof number is:

$$Gr = \left\{ \frac{\text{buoyancy}}{\text{viscous forces}} \right\} = \frac{\beta\, \Delta T\, g\, L^3}{\nu^2} \tag{3.4}$$

Filling in the numbers, with a water temperature at 20 °C, tube temperature of 25 °C and a velocity around 0.1 m/s, results in a value around 35, so natural convection. The Rayleigh number determines if the natural convection is laminar or turbulent regime. The Rayleigh number is expressed as:

$$Ra = \left\{ \frac{\text{buoyancy}}{\text{viscous forces}} \right\} = \frac{\beta\, \Delta T\, g\, L^3\, c_p\, \mu}{\nu^2\, k} \tag{3.5}$$

The Rayleigh number, Ra_L, for the vertical tube is around 10^{12}. The tube dissipates heat into the water.

$$Nu_L = 0.68 + 0.670(Ra_L \Psi)^{1/4} \qquad Ra_L \leq 10^9 \tag{3.6}$$

$$Nu_L = 0.68 + 0.670(Ra_L \Psi)^{1/4}(1 + 1.6 \cdot 10^{-8} Ra_L \Psi)^{1/12} \qquad 10^9 \leq Ra_L < 10^{12} \tag{3.7}$$

where ψ is:

$$\psi = \left[1 + \left(\frac{0.492}{Pr} \right)^{9/16} \right]^{-16/9} \tag{3.8}$$

For the horizontal tube in the vessel:

$$Nu_L = 0.36 + \frac{0.518Ra_D^{1/4}}{[1+(0.559/Pr)^{9/16}]^{4/9}} \qquad 10^{-6} < Ra_D \leq 10^9 \tag{3.9}$$

$$Nu_L = \left[0.60 + 0.387\left[\frac{Ra_D}{[1+(0.559/Pr)^{9/16}]^{16/9}}\right]^{1/6}\right]^2 \qquad Ra_D \geq 10^9 \tag{3.10}$$

where Rayleigh number is in the order of 10^8. The difference in the horizontal and vertical Rayleigh number is defined in the length for vertical tube and diameter for the horizontal tube.

Taking the equations into account for the vertical and horizontal position of the tube, the losses in the tubing will be around 1 kW. The amount of heat entering the system is more than 2 kW. Concluding that this method is not suitable so that a heat exchanger has been chosen.

3.1.2. Selection of pump and flow meter

The pump has been selected for the range of flows which are needed to investigate the local overall heat transfer coefficient. Choosing the inappropriate range may result in inaccurate results or a range where the difference is too small to obtain clear results. Next to this fact, the pump also has to overcome the height and the friction as calculated in section 2.4.1. The pressure drop for the piping system is 14 kPa. The total pressure drop for the heat exchanger is around 30 kPa, this value is provided by the manufacturer. At the flow meter, the pressure drop is negligible. The total pressure drop in the system is around 44 kPa. When the system is open, the height of almost 10 meter, must be taken into account as well. This means, 1 bar of pressure difference from the top to the bottom of the system. At the top, the system is in contact with atmospheric pressure. The pump chosen for this system is the Duijvelaar Pompen type PDLS18-20, centrifugal pump, based on the performance curve. Around 40 Hz, the pressure exceeds 1 bar.
The flow meter has three criteria. The first criteria is the measurement range. For the flow meter, the same range is chosen as the pump. The second criteria is the diameter passage. The pump has an inlet of 50 mm and the tube which is used for the measurements is 63.5 mm. The last but most important criteria is the accuracy of the flow meter. The flow meter chosen is the Altometer K280/6, which is a magnetic-inductive flow meter, with an accuracy of 0.5 percent according to the manufacturer.

3.1.3. Creating a falling film

For the second test, a falling film is created. In order to do so, a collection box (fig. 3.2) is made on the top of the stainless steel tube. The collection box has an inlet on one side of the collection box. Two baffles in between the inlet and outlet flow prevent a straight stream and slows the stream down in the larger volume. To create a falling film, a water buffer is required to achieve a gradual flow over the edge of the outlet tube. The dimensions are given in figure 3.2. For a falling film, the tubes must be aligned perfectly and directed parallel to the gravity force.

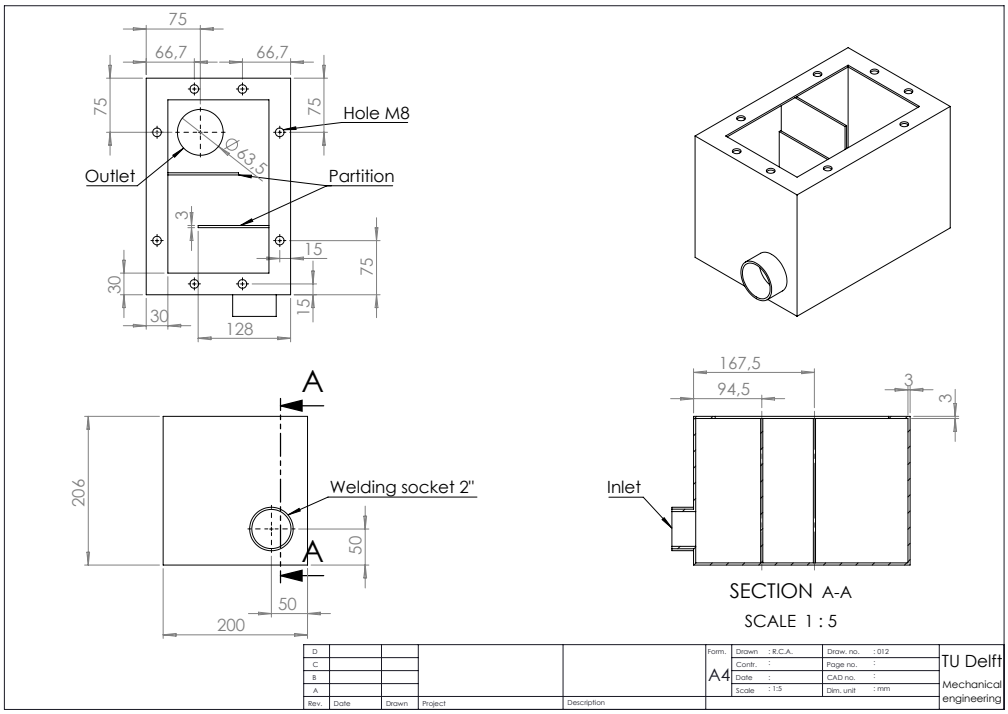

Figure 3.2: Collection box

3.1.4. Heat flux sensor

A heat flux sensor is a sensor which can measure the heat flux. The heat flux is the heat rate per unit area going through the sensor. In the paper of Singh et al. [39], the mounting of the heat flux sensor is discussed. First of all, a general heat flux sensor consists of different layers of substrates and packages, made out of polyamide, Kapton, anodized aluminium or silicone. Furthermore, a heat flux sensor consists of thermopiles, contacts and interconnection. Heat flux sensors are not build for harsh environment such as furnaces, combustion chambers and fires. For a region where condensation takes place, extra attention should be paid. The mounting on the tube's outer surfaces effects the results of the sensor. Those results give a deviation on the expected results. When the heat flux sensor is put into a slot, which has been cut in the tube, it appears that only steady state process can be measured. The paper of Sabau and Wu [40] investigates the process of casting. Although the process is different, the heat flux sensors are also able to measure the heat flux of the process. The conclusion, after measuring the errors in the system, is that the heat flux sensors can successfully be applied by investigation the effects of lubrication, even for different diluted ratios.

This research focus on the conductive heat flux sensors, which is schematically shown in figure 3.3a. This sensor is made out of thermopiles. A thermopile consists of multiple thermocouples placed in series. A thermocouple is made out of two materials and have contact on both their ends. By a temperature difference, the two materials expend differently which causes a voltage difference, presented in figure 3.3b. This principle is called the Seebeck effect.

The Seebeck effect can be described physically as equation 3.11, which links the generated voltage to the temperature:

$$\Delta V = \alpha_s \, \Delta T \tag{3.11}$$

The α_s used in the equation is the Seebeck coefficient which is different for every material pair [41].

(a) General working principle heat flux sensor

(b) Seebeck effect thermocouple

Figure 3.3

To compare the heat flux sensors with each other, the following criteria are taken into account, see table 3.1. To select the heat flux sensor, the heat flux range, the fitting on the tube and the water resistance are important. The heat flux for the falling film evaporator is based on the theory (chapter 2) and the results (chapter 4). The heat flux range is between 2 and 30 kW m^{-2}. The fitting on the tube is not a problem for all of the sensors, they are small or can be bent. For the final application the sensor should be water resistance. All other parameters are in the same order of magnitude. The heat flux sensor of Fluxteq is chosen for the heat flux rate, the bending around the tube and the water resistance. Water resistance is important due to the fact that the sensors are exposed to steam. The ability to measure temperatures is an additional advantage of these sensors.

Table 3.1: Overview heat flux sensors

	Fluxteq	Captex	Greenteg	Hukseflux (Cover band)
Price	$60	€ 107	€ 250	€ 9375
Size [mm]	27x32	10x10	4.4x4.4	140x360
Amount of sensors	Single	Single	Single	Multi
Maximum temperature [°C]	120	200	150	100
Heat flux range [kW m^{-2}]	150	500	150	2
Thermal resistance [K W^{-1} m^{-2}]	$8.64 \cdot 10^{-4}$	$1 \cdot 10^{-3}$	$7.94 \cdot 10^{-4}$	$6 \cdot 10^{-3}$
Fit on tube	Bendable	Yes	Yes	Bendable
Measuring temperature[°C]	Yes	Yes(+ €17)	No	Yes
Delivery time	1-3 days	1 week	2-4 days	4-6 weeks
Water resistance	Water:Yes Steam:Not tested but foreseeing no problem	Water:No Using acrylic coating	Water as long as the sensor is not constantly under water and dried from time to time from the moisture	Yes, Protection class IP65 (low pressure water jets)

3.1.5. Thermal paste

Placing the heat flux sensor against the stainless steel tube will inevitable give a void between the two surfaces due to the roughness of each material. To avoid that the area will be filled with air, which is a well performing insulator, thermal paste is used. Next to the fact that the thermal paste replaces the air, the conductivity of the thermal paste is known. Also, there is a possibility to replace the thermal paste to have a second option to validate the final model. Two thermal paste are used: the Danfoss 'Koperpasta tube AT' and the Arctic Silver 5. Both have a conduction resistance of respectively 0.7 W m^{-1} K^{-1} and 8.9 W m^{-1} K^{-1}. During application of the thermal paste, it is taken into consideration that it should be divided evenly over the heat flux sensor. By placing the heat flux sensor against the tube, the thermal paste must come underneath the heat flux sensor on all sides. Masking tape is used to keep the heat flux sensor at the desired place when mounting the heat blanket. The masking tape is placed at the position on the heat flux sensor where there is no measurement. The measurement is done in the inner region of the heat flux sensor. The following figure shows the result.

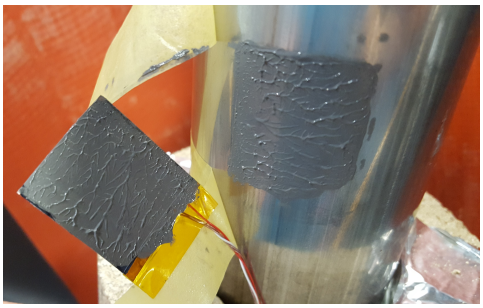

Figure 3.4: Thermal paste Arctic Silver 5 between heat flux sensor and tube

3.2. Measurement area

The beginning of the measurement area is located at 4.3 meter from the inlet of the stainless steel tube, so the velocity profile of the water will be developed. Furthermore, a heat blanket is used which means that the surface receives an uniform heat flux. The heat blanket is a flexible silicon blanket with a wire inside for the heating. The advantage of the flexibility is that it can be bound around the tube. The disadvantage of the heat blanket is that it is built up from five vertical strokes. In between the strokes, it is not heated. In the strokes it is assumed that the heating is homogeneous. However, the wire inside the silicon blanket is placed horizontal so it makes a turn on the edges of the stroke.

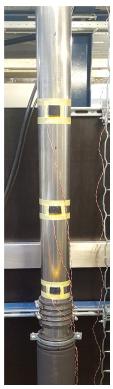

(a) Tube with heat flux sensors

(b) Tube with heat blanket

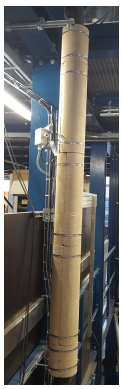

(c) Tube with insulation

Figure 3.5: Measurement area

A schematic overview is given in the figure below with the position of the sensors at the outside of the medium-carrying tube. The heat blanket has a total length of 1.500 mm and is placed over all the heat flux sensors. The flow is fully developed in this area. The direction of flow is from top to bottom. The distance of the heat flux sensors is measured from the bottom side of the heat blanket. The numbers of the sensors are adopted from the number of the certificates of the manufacture. Heat flux sensor 6 is placed at the bottom of the heat blanket and heat flux sensor 14 is placed at the top of the heat blanket. Heat flux sensor 10 is placed around the middle of the heat blanket, and heat flux sensor 7 is placed at 300 mm from the bottom side of the heat blanket. Insulation is mounted around the heat blanket. Above and below the measurement area, the temperature is measured with type K sensors. The data of the temperature sensors have been read out by a process transmitter from Endress + Hauser using LabVIEW. The signals generated by the heat flux sensors are processed by a FluxDAQ converter. This device converts the DC voltage signals of the heat flux sensors into temperature and heat flux values.

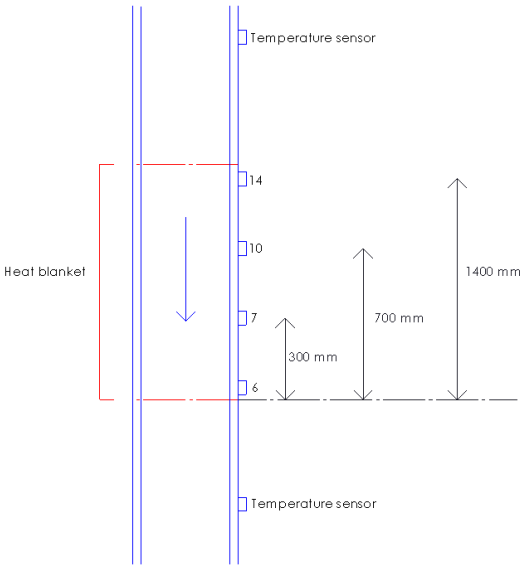

Figure 3.6: Overview measuring area

3.2.1. Insulation

Two types of insulation are used in the experimental setup. The mean reason for using two different types is the temperature reached by the heat blanket. The first type is Armaflex AF and is used one meter above and one meter below the measuring area. The thermal conductivity value is 0.033 W m^{-1} K^{-1} and the maximum operation temperature is 110 °C [42].
The tube temperature is taken as 25 °C, the outside temperature as 15 °C and the velocity of the wind as 1 m/s. Because air is the medium, the transition from natural convection to forced convection is slightly different. So, for Prandtl around 1:

$$\text{Forced convection} \qquad \frac{Gr}{Re^2} \ll 1 \tag{3.12}$$

$$\text{Mixed convection} \qquad \frac{Gr}{Re^2} \approx 1 \tag{3.13}$$

$$\text{Natural convection} \qquad \frac{Gr}{Re^2} \gg 1 \tag{3.14}$$

Therefore, mixed convection occurs as the value of 0.67 which is about 1.

Mixed convection consists out of natural convection and forced convection, which is connected with the following relation [23]:

$$(\overline{Nu} - \overline{Nu}_0)^3 = (\overline{Nu}_f - \overline{Nu}_0)^3 + (\overline{Nu}_n - \overline{Nu}_0)^3 \tag{3.15}$$

where $\overline{Nu}_0$ is zero for plates, which approaches the vertical tube the most. $\overline{Nu_n}$ is the natural convection and both equation 3.6 and equation 3.7 are used. For $\overline{Nu_f}$, the tube can be seen as a cylinder. The airflow is assumed to be flowing horizontally through the lab to cool the tube. The Nusselt number is based on the correlation proposed by Churchill and Bernstein [43].

$$\overline{Nu}_D = 0.3 + \frac{0.62 Re_D^{1/2} Pr^{1/3}}{[1 + (0.4/Pr)^{2/3}]^{1/4}} \qquad Re_D < 10^4 \tag{3.16}$$

$$\overline{Nu}_D = 0.3 + \frac{0.62 Re_D^{1/2} Pr^{1/3}}{[1 + (0.4/Pr)^{2/3}]^{1/4}} \left[1 + \left(\frac{Re_D}{282000}\right)^{1/2}\right] \qquad 2 \cdot 10^4 < Re_D < 4 \cdot 10^5 \tag{3.17}$$

$$\overline{Nu}_D = 0.3 + \frac{0.62 Re_D^{1/2} Pr^{1/3}}{[1 + (0.4/Pr)^{2/3}]^{1/4}} \left[1 + \left(\frac{Re_D}{282000}\right)^{5/8}\right]^{4/5} \qquad 4 \cdot 10^5 < Re_D < 5 \cdot 10^6 \tag{3.18}$$

The amount of heat lost without insulation has been calculated at 15 W. The heat loss with insulation is around 6 W, when the thickness of the insulation is set at two centimetres. In this equation the tube temperature is set at 25°C. The temperature difference is small so it will not be taken into account.

For the heat blanket, Pumica is used for insulation. Pumica is made out of ceramically-bonded Vermiculite dishes [44]. The maximum temperature which it can withstand is 900 °C. The thermal conductivity is 0.125 W m^{-1} K^{-1} and the density is 500 kg/m^3. The thickness of the Pumica is 8 cm.

3.3. Construction of the setup

Using the P&ID from section 3.1, the ground part in figure 3.7 has the following components. The tank (white), the pump on the ground floor (blue) and the heat exchanger on the left front of the picture (grey). The blue flow meter can be seen on the top of the figure. Furthermore, it can be seen that the stainless steel tube coming from the measurement section enters the picture in the middle. For the top part (fig. 3.8), the collection box, the pressure safety valve and the air vent are visible. On the ground, the other parts of the setup can be seen. The measurement area is roughly located in the middle.

Figure 3.7: Ground parts of experimental setup

Figure 3.8: Total experimental setup

3.4. Heat transfer in measuring area

The input for calculating the local overall heat transfer coefficient are the temperature sensors and the heat flux sensor with temperature sensors as well. The equation used for the experimental calculation of the overall heat transfer coefficient is the following:

$$U = \frac{q}{\Delta T} \tag{3.19}$$

The equation is not divided into the principles of heat transfer as discussed in section 2.1, but shows directly the overall heat transfer coefficient. To compare the overall heat transfer with theory, the model in figure 2.10 is made from the heat flux sensor to the water in the tube. Figure 2.12 shows the resistances for the overall heat transfer coefficient, which are calculated individually. Both experimental and theoretical overall heat transfer coefficients are known, so the comparison can be made.

3.5. Signal noise

In the beginning of the experimental tests, the heat flux sensors had a small signal to noise ratio in the signal. The cables of the heat flux sensors are not insulated, so the noise can be produced outside the setup and influence the signal of the heat flux sensor. To analyse noise from external factors, a Fast Fourier Transform (FFT) has been executed.

Performing an FFT on the measured data, the FFT provided no clear results. To find the source of the noise, the sensor was detached from the setup. It appears that the heat blanket, using alternating current, has influence on the cable of the heat flux sensor. Figure 3.9 shows the noise of the heat flux sensor. The heat flux sensor itself is mounted below the heat blanket. The first 50 seconds have an acceptable signal to noise ratio for the temperature of the heat flux sensor (fig. 3.9). After that time, the heat blanket starts to produce heat.

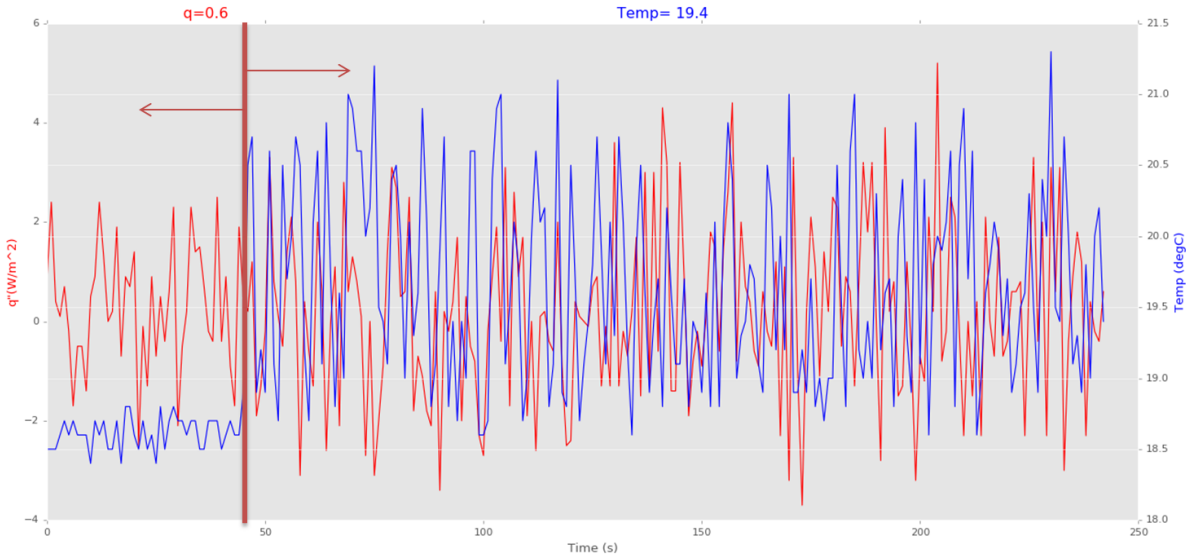

Figure 3.9: Heat flux (red) and temperature (blue) of heat flux sensor plotted over time. At 50 seconds, wire of heat flux sensor over heat blanket. Left of the vertical line is an acceptable signal to noise ratio. On the right of the vertical line an unacceptable signal to noise ratio, the cable crosses the heat blanket using alternating current.

The sensor is far away from the heat blanket, so there is no temperature or heat flux increase. To check the influence of the heat flux sensor itself, the heat flux sensor is attached to the heat blanket. The noise was not as visible as the noise of the wire over the heat blanket. The noise can be explained by the cable which is attached to the sensor (fig. 3.10a).

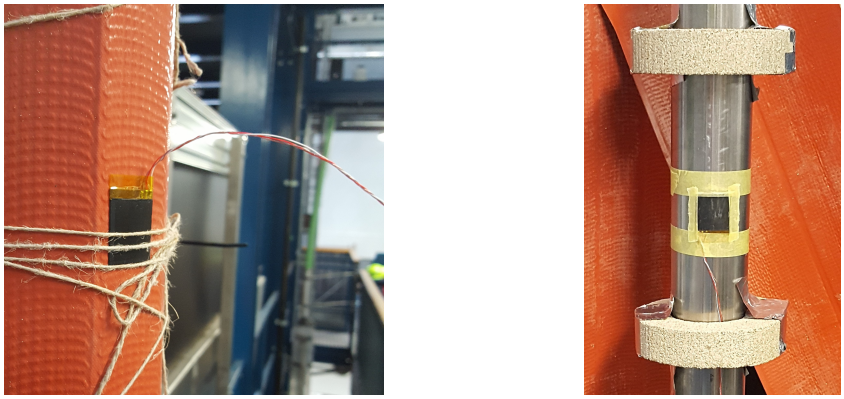

(a) (b)

Figure 3.10: (a) Heat flux sensor attached to heat blanket and (b) heat flux sensor spacing to heat blanket

Having space between the heat flux sensor and the heat blanket was the first solution to reduce noise of the heat blanket (fig. 3.10b). The sand coloured rings are used to keep a constant distance between the sensor and the heat blanket. Furthermore, the rings are not placed too far from each other to avoid circulation of air between the hot surface of the heat blanket and the cold surface of the tube. The results of the sensors were not as good as expected. Because insulation was not used, the environment had a large influence on the heat blanket and on the results.
The second solution is to use direct current (DC) instead of alternating current (AC). As shown in figure 3.10a, the heat blanket is built up by wires close to each other. These wires can potential form a coil which gives a flux by alternating current. At direct current, the fluctuations do not appear. Direct current (DC) produced by a power supply of Delta Elektronika type SM 120- 25 D, is used in further experiments.

4

Results

This chapter is divided in two sections. The first section describes the results of the theoretical approach of the falling film evaporator used by FrieslandCampina. These results of the falling film evaporator are needed to determine the heat flux. With the heat flux range known, the heat flux sensors can be selected, see section 3.1.4. In the second section, the heat flux sensor will be investigated in an experimental setup and the results are described here.

4.1. Falling film evaporator: theoretical approach

In order to calculate the falling film in the evaporator, several restrictions are taken into account. These restrictions preserve the quality of the milk powder. The evaporation temperature of the water is 70 °C, due to an under pressure in the tube. The maximum temperature of the outer wall is 77 °C to prevent nucleation boiling. The mass flow rate per unit width γ is 900 kg m^{-1} h^{-1} and the total length of the tube is 54 meter. The concentration varies with the position in the tube because the water evaporates. The milk is assumed to consists of 80 percent water, from which only 60 percent has to be evaporated to obtain a 60 percent dry concentration of milk.
Next, the falling film and the tube wall are included in the calculations. However, the vapour inside the tube and the steam on the outside are *not* taken into account. These can vary and is specific to the installation itself. The focus of this report is the falling film inside the tube.

With the theory for a falling film described in chapter 2, the results are presented for the given input values. Starting with the relation between the Reynolds number and the position along the tube (fig. 4.1a). It appears that the Reynolds number decreases for increasing position of the fluid into the evaporator. The reason is that the water evaporates, so the density and the kinematic viscosity are changing, diameter is constant and the change in velocity is small. The density differs for milk to milk powder with respectively 978 kg/m^3 and 1315 kg/m^3. The kinematic viscosity has the largest influence of the four properties (tab.4.1). The horizontal axis represents the position in the tube, while the vertical axis the Reynolds number is shown. Figure 4.1b shows the Reynolds number in log scale. The small values become visible as well.

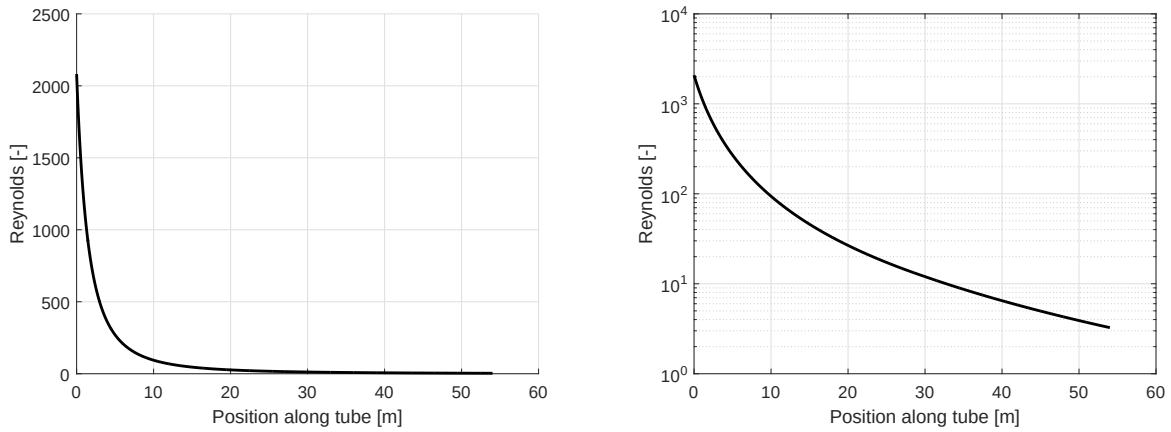

(a) (b)

Figure 4.1: (a) Reynolds number over the position in the tube and (b) Reynolds number on log scale over the position in the tube

The importance of kinematic viscosity is shown in table 4.1. The range for solid dry mass is in the range of 10 percent to 60 percent, while the kinematic viscosity changes in this range with a factor of almost 1000.

Table 4.1: Property of the kinematic viscosity [28]

Solid dry mass [kg kg^{-1}]	Kinematic viscosity [mPa]
0.1	0.47
0.29	8.2
0.45	40
0.55	250
0.62	400

The solid dry mass along the position in the tube is plotted to indicate where the evaporation has the most effect. Furthermore, the kinematic viscosity can be coupled to the position of the tube by the use of table 4.1.

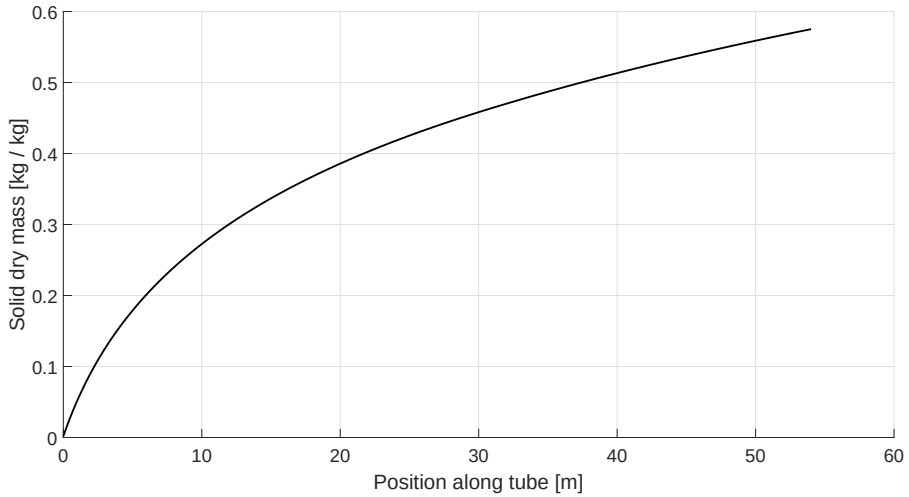

Figure 4.2: Solid dry mass over the position in the tube

The falling film evaporators should be able to produce 60 percent of dry concentration of milk. With the given restrictions, the amount of mass flowing through the tubes is plotted (fig. 4.3). In the beginning of the tube, no evaporation has taken place and so the mass is equal to the amount flowing in from the top. When the milk is flowing through, the water is slowly evaporated from the milk and the amount of mass decreases. As a result, the concentration of solid dry mass of milk is increasing. The incoming mass is roughly 0.048 kg/s, the amount of mass leaving the falling film evaporator is 0.024 kg/s. 60 percent of dry concentration is equal to a mass leaving the system of 0.023 kg/s. The small difference could be caused by the vapour flow inside the tube, which has not been taken into account.

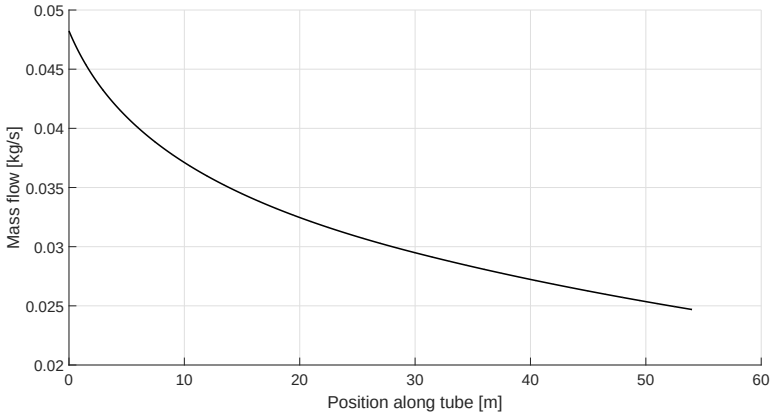

Figure 4.3: Mass flow over the position in the tube

In the next diagram is the heat flux at each location of the tube (fig. 4.4a). The heat flux (horizontal axis) and the vertical axis is similar as in the previous diagrams. However, interesting is the change in the transition regime from wavy laminar to laminar. This is a general accepted threshold of Reynolds number 30 given by water. Milk has different properties. The Reynolds number is shown in figure 4.1b. When going from a constant Reynolds number of 30 (fig 4.4a), to a constant of Reynolds number of 12 (fig. 4.4b), the jump disappears. Apparently, the milk has a different influence on the falling film than water. The transition from wavy laminar to laminar shifts. The generally accepted threshold of Reynolds number 30 has to be adjusted. From the heat flux, the range of the heat flux sensors is selected.

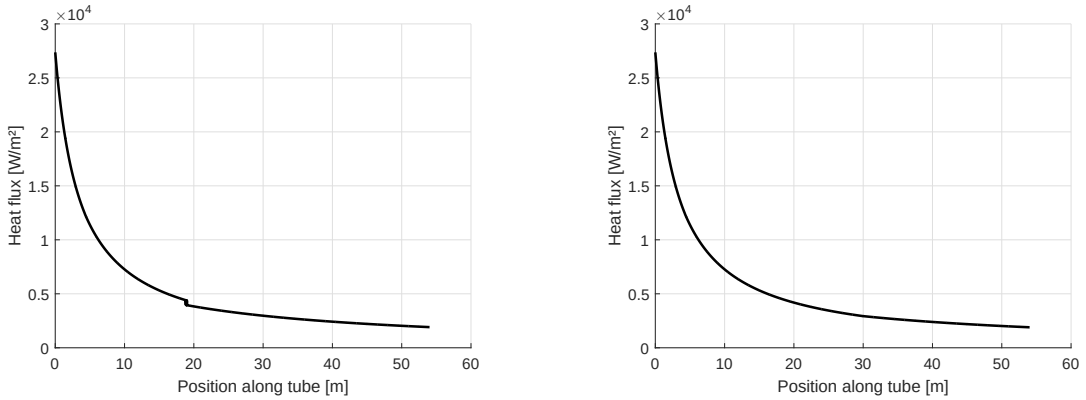

Figure 4.4: Relation between the heat flux and the Reynolds number at (a) Reynolds number 30 and (b) Reynolds number 12

The last diagram (fig. 4.5) contains the overall heat transfer coefficient of three different mass flows per unit width. Before selecting the heat flux sensors, the difference between the overall heat transfer coefficient is investigated to determine if the difference is large enough to distinguish the mass flow in the tube. Comparing the mass flows, the mass increases by 0.01 kg/s at every 200 kg m^{-1} h^{-1} increase. The difference in mass flow is small, however, the overall heat transfer coefficient can be distinguished. At a position of 10 meter along the tube, the overall heat transfer coefficient is at {700, 900, 1100} kg m^{-1} h^{-1} respectively, {790, 930, 1075} W m^{-2} K^{-1}. In general, the range of the overall heat transfer coefficient is between the 200 W m^{-2} K^{-1} and 3000 W m^{-2} K^{-1}. The overall heat transfer coefficient decreases because of the thermal resistance of the falling film increases due to the solidifying of milk. For the determination of the error margin, the selected heat flux sensor and temperature sensor are taken into account. At the position of 10 meter and for a mass flow per unit width of {700, 900, 1100} kg m^{-1} h^{-1} is the error margin respectively ± {40.5, 47.6, 54.9} W m^{-2} K^{-1}. The error margin is based on the selected heat flux sensor and temperature sensor in the experimental setup.

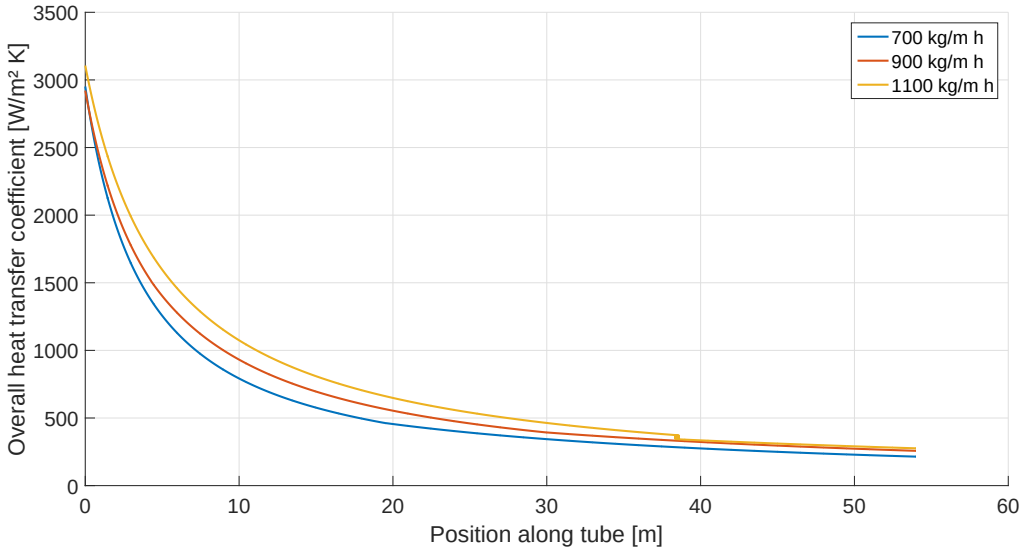

Figure 4.5: Overall heat transfer coefficient over the position in the tube at mass flows per unit width of 700 kg m^{-1} h^{-1}, 900 kg m^{-1} h^{-1} and 1100 kg m^{-1} h^{-1}

4.2. Heat flux sensors: Experimental approach

To investigate the heat flux sensors, there are experiments performed with the full water flow in the tube. The variations in this experimental setup are (i) the power input, (ii) the thermal paste, (iii) the position of the heat flux sensors and (iv) the honeycomb structure at the inlet of the tube have been changed during the tests. The experiments are compared with the theoretical prediction and the reliability of the experiment is investigated as well.

4.2.1. Variable 1: Power input

Four heat flux sensors are used, each at different places on the tube (fig. 3.6). Figures 4.6a to 4.6d give the results of the local overall heat transfer coefficients at the location of the four heat flux sensors. The thermal paste used for these results is Danfoss 'Koperpasta tube AT' with a conductivity of 0.7 W m^{-1} K^{-1}. For all the diagrams, the vertical axis is set at 100 to 400 W m^{-2} K^{-1} to have a better comparison. The flow rate (horizontal axis) ranges from 0 to 3.5 l/s. The theoretical curve is calculated from the electrical analogy of the system at 1500 W, while the points are experimental

data. The power inputs are 200 W, 400 W, 800 W and 1500 W. The predicted theoretical curve ranges from a Reynolds number of 10000 to a Reynolds number of 10^5 (3.5 l/s). Below Reynolds number 10000 the transition regime is present. The transition region is not well described by literature, which makes it inaccurate to compare.

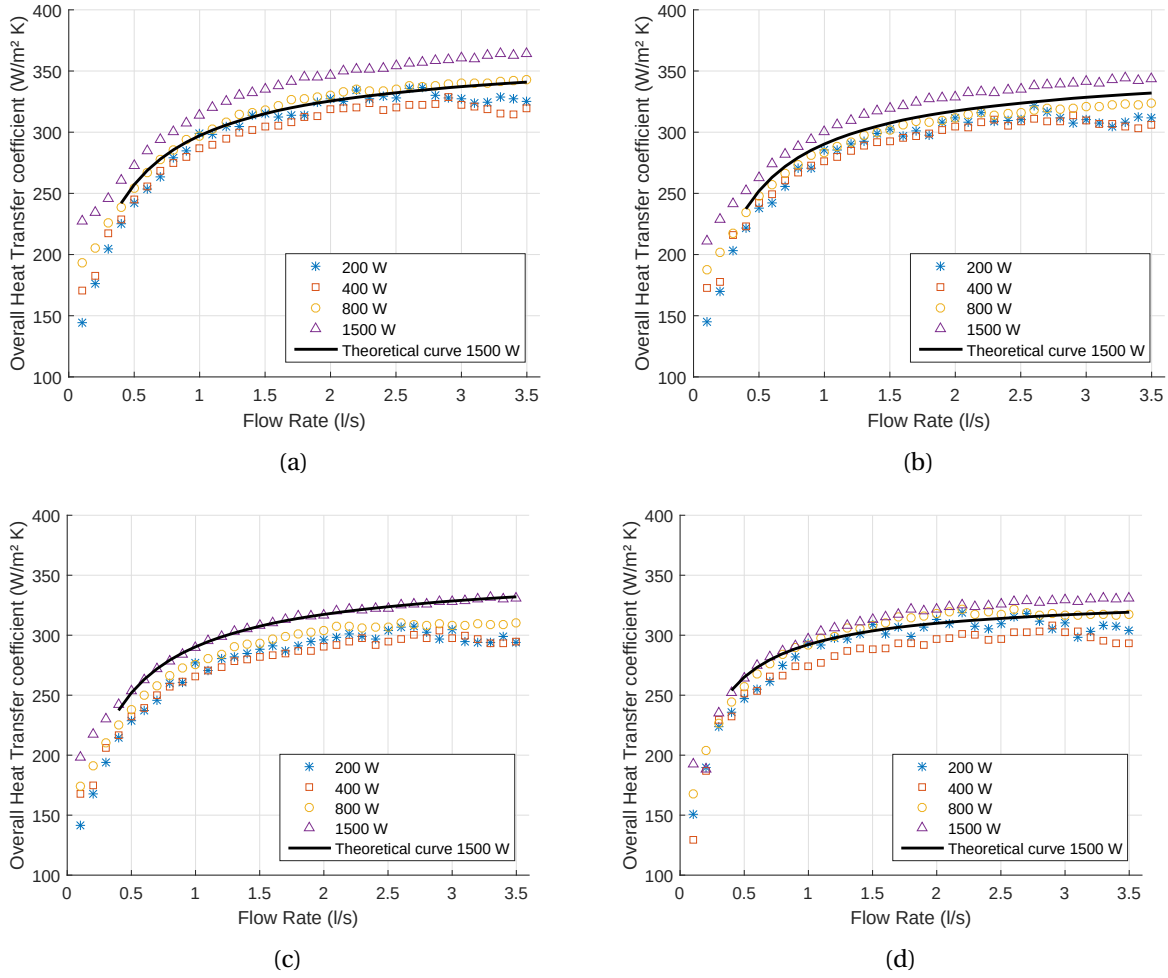

Figure 4.6: Local overall heat transfer coefficient at the location of the heat flux sensors with thermal paste Danfoss 'Koperpasta tube AT' and power input 200 to 1500 W. (a) heat flux sensor 6, thermal paste thickness of 0.03 mm (b) heat flux sensor 7, thermal paste thickness of 0.05 mm (c) heat flux sensor 10, thermal paste thickness of 0.05 mm (d) heat flux sensor 14, thermal paste thickness of 0.11 mm

By studying the diagrams, four clear observations can be made concerning the:
- entry length
- power input
- difference between heat flux sensor 7 and 10
- 200 W power input

Heat flux sensor 14 is positioned at the entrance of the heat blanket. The results of heat flux sensor 14 (fig. 4.6d), has already the term Nu_x/Nu_{inf} included for the entry length. Mills set this entry length term to 1.8 in his theoretical analysis. To have a better fit with the experimental data, it is chosen to use a term of 1.5. To compare this term with the normally used convection equation, both are plotted in figure 4.7. It shows that the curve of this term is more step at lower flow rates. At higher flow rates, the curve is more flatted out in comparison with the normal used convection equation.

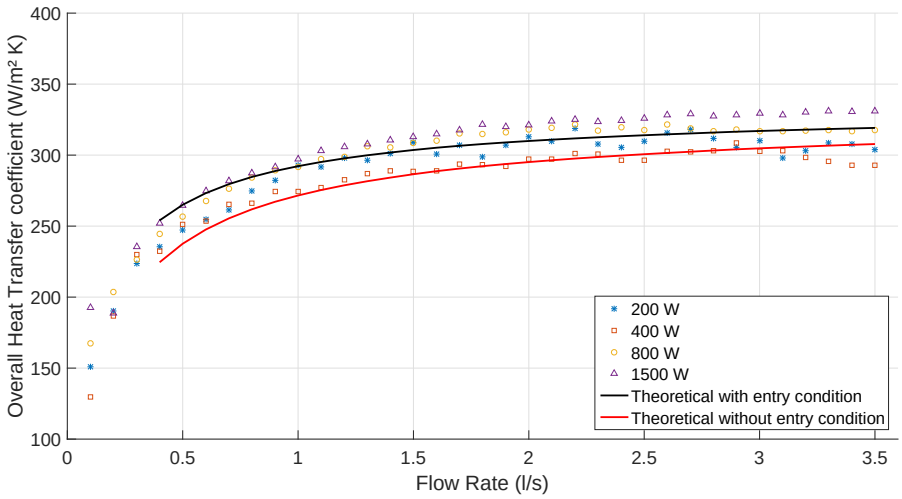

Figure 4.7: Local overall heat transfer coefficient at position heat flux sensor 14 with Danfoss 'Koperpasta tube AT', thickness 0.11mm. With and without correction entry length

Diagram 4.6a to 4.6c shows that at lower power input, the local overall heat transfer coefficient is lower as well. To compare this result with literature, the theoretical curve is calculated for a power input of 200 W and 1500 W (fig 4.8). As can be seen, the difference is not as large as the experimental results. For the theoretical curve, only the resistance through the water changes due to the heating of the water. It is visible that the line of 1500 W starts at 0.4 l/s and 200 W at 0.5 l/s due to the fact that the theoretical curve starts at a Reynolds number of 10,000. For the experimental results, a combination of the heat flux and temperature difference across the tube are relevant.

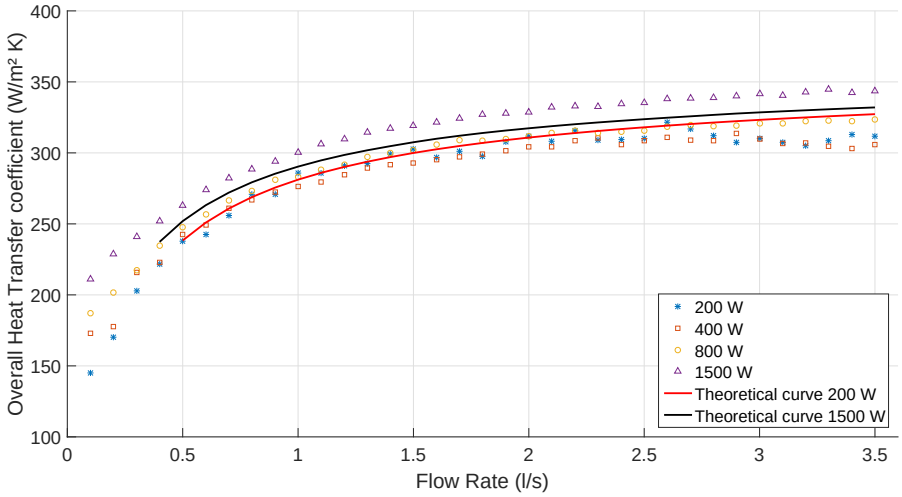

Figure 4.8: Local overall heat transfer coefficient at position heat flux sensor 7 with Danfoss 'Koperpasta tube AT', thickness 0.05mm. Theoretical curve plotted at 200 W and 1500 W.

The local overall heat transfer coefficient consists of the temperature difference and the heat flux. In figure 4.9b, the temperature difference of heat flux sensor 7 and 10 are plotted. The temperature difference is measured over the temperature sensor of the heat flux sensor and the temperature sensor on the bottom of the measurement area. The added heat from the heat blanket at the position of the heat flux sensor to the end of the heat blanket is taken into account, as well as the difference in the offset. Shortly, the temperature at the middle of the water is taken into account at same height where the heat flux sensor is attached to the tube.

Figure 4.9a presents the heat flux at a power input of 1500 W. It is clearly visible that there is a gap in the experimental heat flux data between heat flux sensor 7 and sensor 10. To calculate the local overall heat transfer coefficient, the temperature difference is taken into account. It can be seen that there is a temperature difference gap between heat flux sensor 7 and heat flux sensor 10, just as by the heat flux. Therefore, there are only slight difference but no unexpected differences in the local overall heat transfer coefficient.

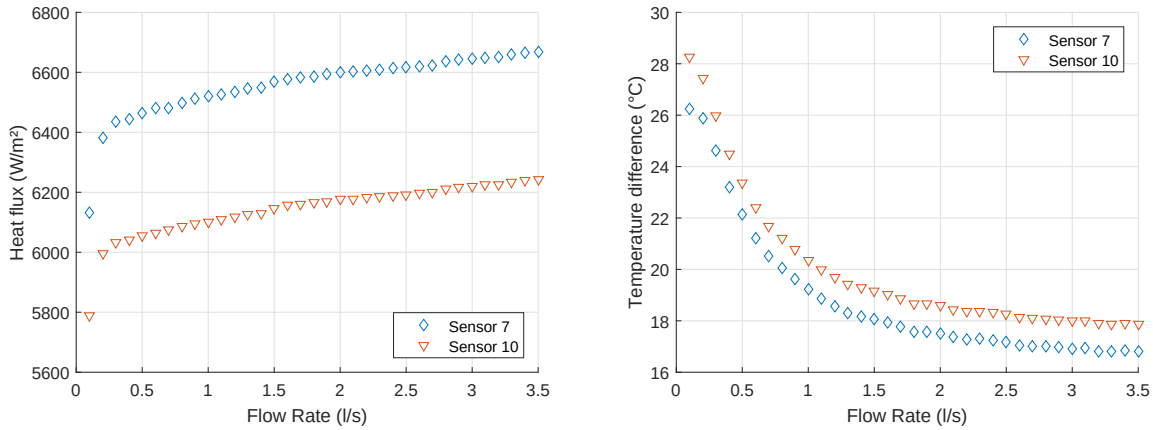

(a) (b)

Figure 4.9: Temperature difference from heat flux sensor to inside water (a) and heat flux of heat flux sensor and (b) at position of heat flux sensor 7 and 10 with thermal paste Danfoss 'Koperpasta tube AT', thickness respectively 0.05 mm and 0.05 mm, at 1500 W

Measuring the heat input can be done with a third method. Next to the source for the power input of the heat blanket and the heat flux sensors themselves, the heat input can be measured by the temperature increase of the water. As described in section 3.1, there are two temperature sensors. The first temperature sensor is placed before the water flow passes the heat blanket, the second temperature sensor is after the heat blanket. Figure 4.10 shows the calculated heat input from the temperature sensors. It can be concluded that the measured data is too inaccurate to draw a proper conclusion. The reason for the inaccuracy is the small temperature difference between both the sensors. At 0.1 l/s, the difference is still 2.3 °C, and at 3.5 l/s, the difference is just 0.18 °C. In the diagram, the temperature difference is fluctuating between 0.13 °C and 0.32 °C.

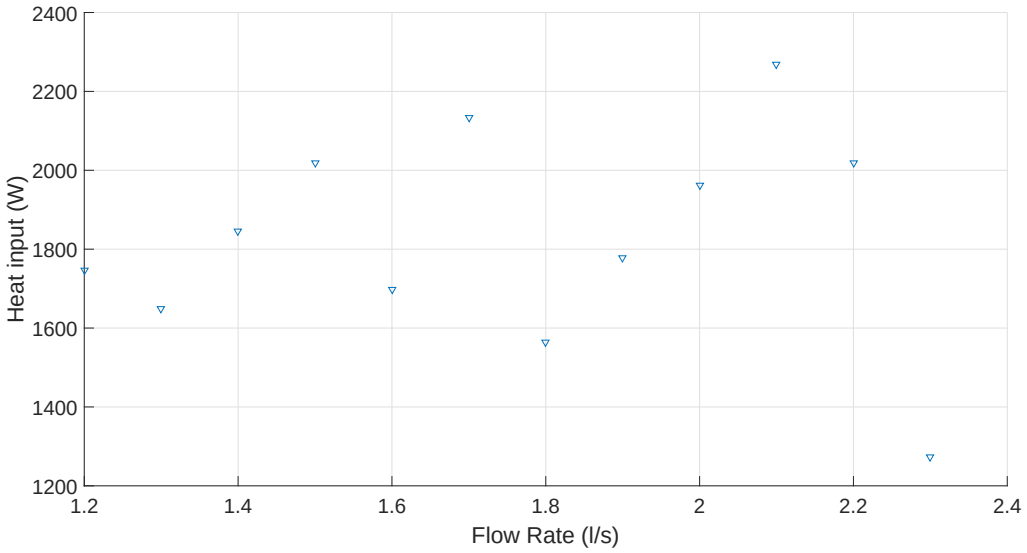

Figure 4.10: Amount of heat at 1500 W measured by two temperature sensors at the top and bottom of the measurement area

The fluctuation in the local overall heat transfer coefficient of 200 W is the last observation. It appears from figure 4.11a that the temperature difference becomes small, around 2.3 °C. The accuracy of the sensors influence the results. The range for the heat flux is small (fig. 4.11b), except from the first value at 0.1 l/s. A possibility for this range is the source of the power input. The power difference is just 6 W.

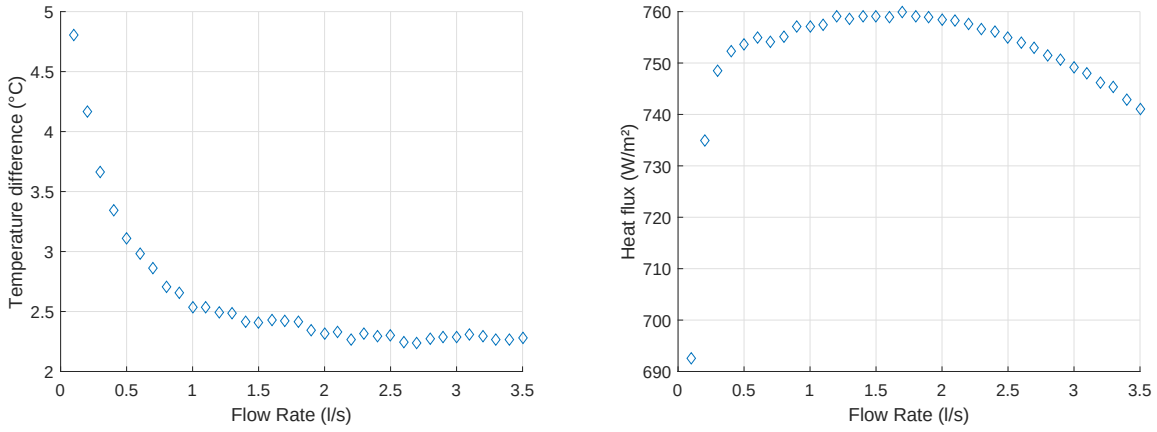

(a) (b)

Figure 4.11: Position of heat flux sensor 6 with thermal paste Danfoss 'Koperpasta tube AT', thickness 0.03 mm, at 200 W (a) temperature difference from heat flux sensor to inside water and (b) the heat flux of heat flux sensor

4.2.2. Variable 2: Thermal paste

The second variation is the thermal paste. The thermal paste is changed from Danfoss 'Koperpasta tube AT' to Arctic Silver 5 with a thermal conductivity of 8.9 W m^{-1} K^{-1}. To investigate the influence of the thermal paste (fig. 4.12a to fig. 4.12d), the local overall heat transfer coefficient is given at the position of the heat flux sensors 6 to 14. For heat flux sensor 6, 7 and 10, the vertical axis is set from 100 to 450 W m^{-2} K^{-1}, heat flux sensor 14 is set to 550 W m^{-2} K^{-1}. The horizontal axis is similar

as in the diagrams which are shown before. The heat input is from 400 W to 2000 W. The diagrams already shown a fluctuation at 400 W, so it is decided to use 2000 W instead of the 200 W. The heat blanket has a maximum power of 2300 W, so it is not possible to double from 1500 W.

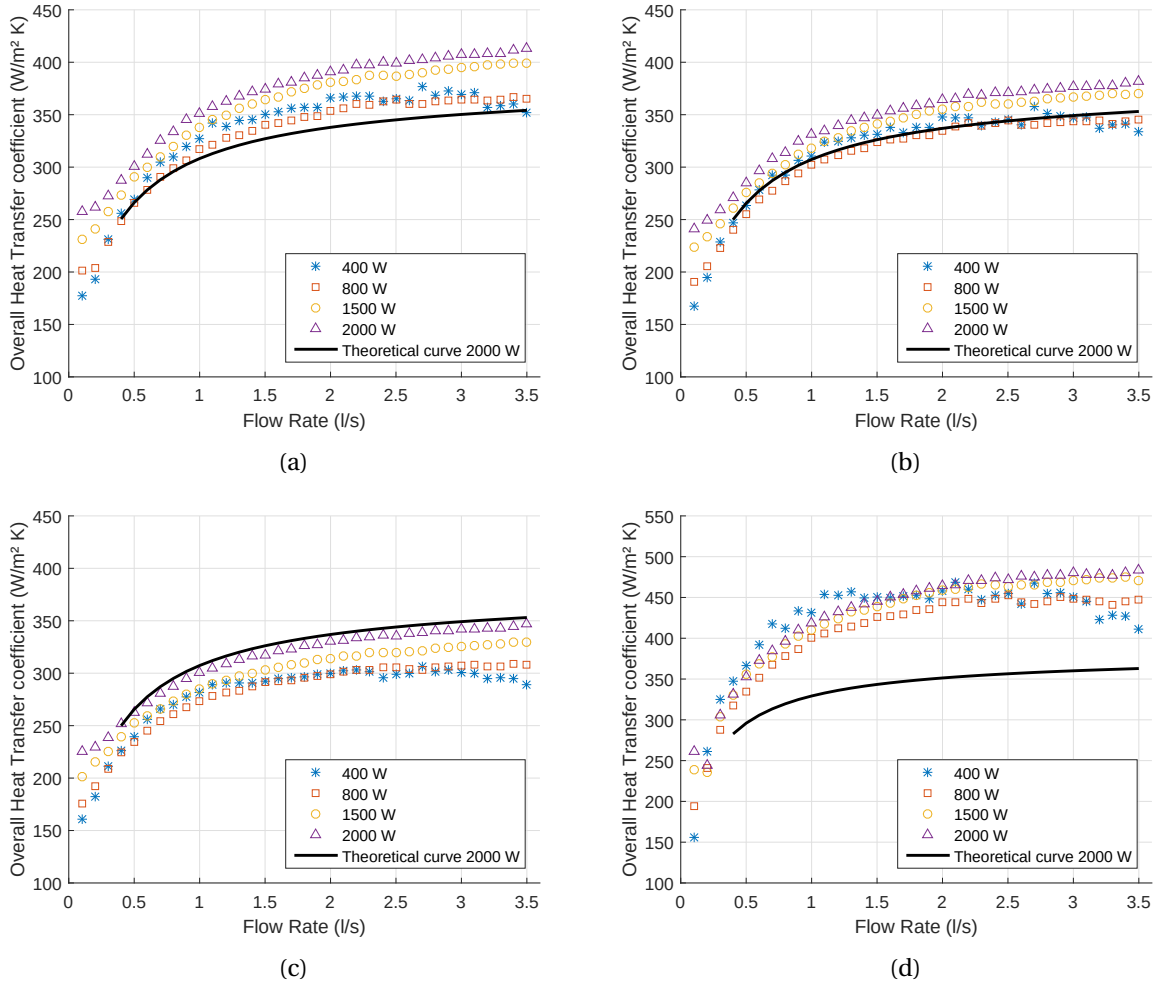

Figure 4.12: Local overall heat transfer coefficient at the location of the heat flux sensors with thermal paste Arctic Silver 5 and power input 400 to 2000 W. (a) heat flux sensor 6, thermal paste thickness of 0.03 mm (b) heat flux sensor 7, thermal paste thickness of 0.05 mm (c) heat flux sensor 10, thermal paste thickness of 0.05 mm (d) heat flux sensor 14, thermal paste thickness of 0.11 mm

The measured data with the Arctic Silver 5 is not as good in comparison as the thermal paste of Danfoss 'Koperpasta tube AT'. Furthermore, it can be seen that the local overall heat transfer coefficient decreases from the position of heat flux sensor 6 to heat flux sensor 10. The entry length, positioned at heat flux sensor 14, follows the same curve as the theoretical analysis, however the data points are not in the range. A comparison between heat flux sensor 10 and 14 is made as well.

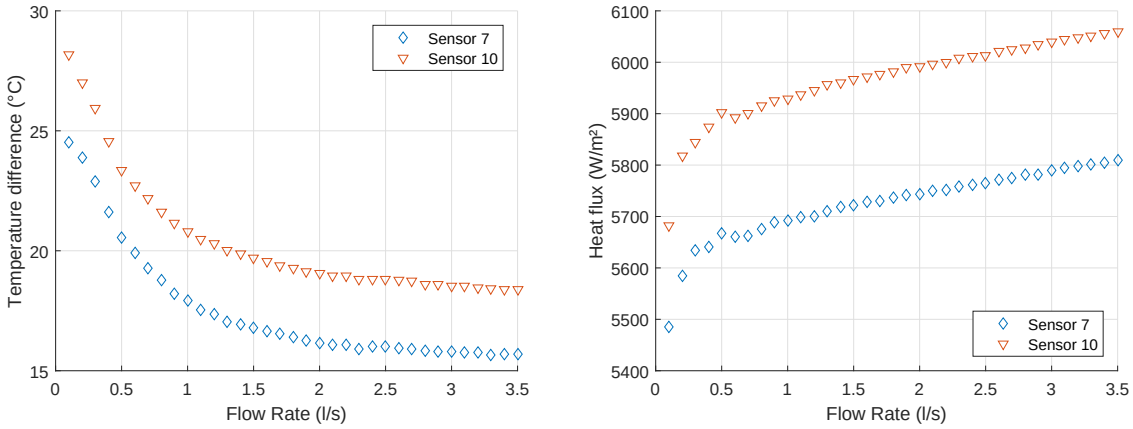

(a) (b)

Figure 4.13: Position of heat flux sensor 7 and 10 with thermal paste Arctic Silver 5, thickness respectively 0.05 mm and 0.05 mm, at 1500 W (a) temperature difference from heat flux sensor to inside water and (b) heat flux of heat flux sensor

Analysing heat flux sensor 7 and 10, the temperature as well as the heat flux, the curves are not overlapping. Comparing with figure 4.9b and figure 4.9a, the temperature difference increases. This explains why the local overall heat transfer coefficient decreases from heat flux sensor 7 to heat flux sensor 10. The temperature difference drop can be originated to the heat flux sensor.
A comparison is made between heat flux sensor 10 and 14 (fig. 4.14a - fig. 4.14b). The temperature difference and heat flux are not overlapping, as what is expected. The heat flux of sensor 14 is lower with 25 percent, however the temperature difference has the largest influence with 76 percent on the local overall heat transfer coefficient.

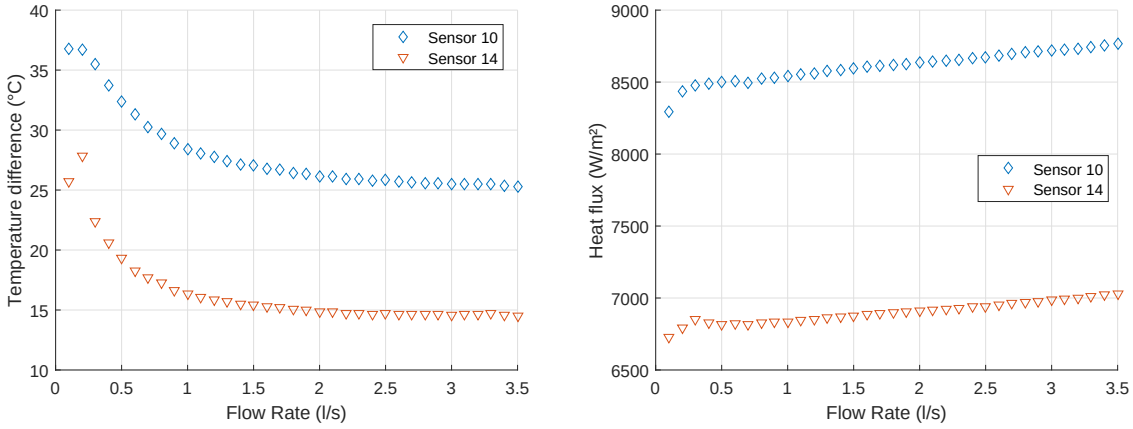

(a) (b)

Figure 4.14: Position of heat flux sensor 10 and 14 with thermal paste Arctic Silver 5, thickness respectively 0.05 mm and 0.11 mm, at 1500 W (a) temperature difference from heat flux sensor to inside water and (b) heat flux of heat flux sensor

Studying the temperature of the heat flux sensors, the difference in the temperature difference can be clarified. In the table below, the temperatures of the heat flux sensors are listed at 2 l/s. Having a good comparison, the heat flux sensor with thermal paste Danfoss 'Koperpasta tube AT' are taken in account as well. The power input is 1500 W.

Table 4.2: Temperature of the heat flux sensors at 2 l/s with a power input of 1500 W with thermal paste of Danfoss 'Koperpasta tube AT' and Arctic Silver 5

Sensor	Temperature heat flux sensor with Arctic Silver [°C]	Temperature heat flux sensor with Danfoss [°C]
6	44.4	47.8
7	45.2	50.0
10	48.1	49.4
14	39.4	45.3

Having a closer look at the temperature difference at the position of heat flux sensor 10 from figure 4.14a, the bulk temperature and temperature of the heat flux sensors are shown in table 4.3. At low flow rates, the temperature of the heat flux sensor decreases from 61 °C to 56 °C. This can be explained by the fact that more heat can be transported to the water due to the fact that the velocity is increasing. However, the bulk temperature is increasing as well and so the temperature difference becomes smaller. This results in a temperature increase of the heat flux sensor after 1 l/s. As can be seen at the previous figure, the total temperature difference becomes smaller.

Table 4.3: Temperature of the heat flux sensors and bulk temperature of the fluid at 2000 W at a flow rate between 0.1 to 3.5 l/s

Flow rate [l/s]	Temperature heat flux sensor [°C]	Temperature bulk water [°C]	Flow rate [l/s]	Temperature heat flux sensor [°C]	Temperature bulk water [°C]	Flow rate [l/s]	Temperature heat flux sensor [°C]	Temperature bulk water [°C]
0.1	58.7	21.9	1.3	56.8	29.4	2.5	59.5	33.6
0.2	61.1	24.4	1.4	56.9	29.7	2.6	60.0	34.3
0.3	59.5	24.0	1.5	57.2	30.1	2.7	60.3	34.6
0.4	58.8	25.1	1.6	57.2	30.5	2.8	60.6	35.0
0.5	57.6	25.3	1.7	57.5	30.8	2.9	61.0	35.4
0.6	57.2	25.9	1.8	57.6	31.2	3.0	61.4	35.8
0.7	56.6	26.3	1.9	57.9	31.6	3.1	61.7	36.2
0.8	56.6	26.9	2.0	58.1	31.9	3.2	62.0	36.6
0.9	56.4	27.5	2.1	58.4	32.2	3.3	62.5	37.0
1.0	56.2	27.9	2.2	58.5	32.7	3.4	63.2	37.8
1.1	56.5	28.4	2.3	58.8	32.9	3.5	63.6	38.3
1.2	56.5	28.8	2.4	59.2	33.4			

4.2.3. Variable 3: Change of position

In the previous diagrams of the local overall heat transfer coefficient, the trend could be notified that the location of the heat flux sensor has an effect on the result. Therefore, heat flux sensor 7 and 10 have changed position to investigate this possible influence. The used thermal paste for both setups is Arctic Silver 5. Figure 4.15 is the result of the change of position. Heat flux sensor 10 gives an expected result and shows the independence of position. Heat flux sensor 7 differs from the theoretical value more than earlier measurements. A possible explanation is that the heat blanket has been taken off and put back on again.

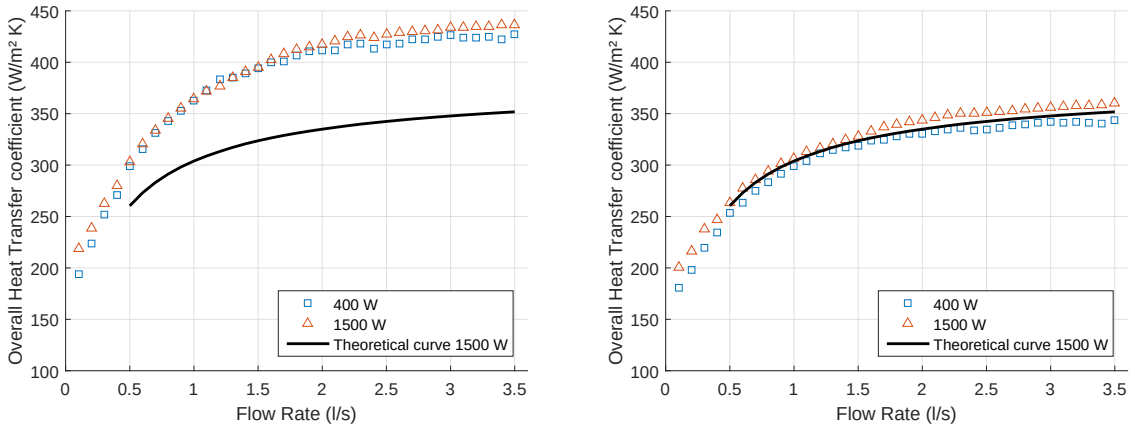

Figure 4.15: Local overall heat transfer coefficient over the flow rate. Thermal paste is Arctic Silver 5 with a power input of 400 W and 1500 W. (a) Position of heat flux sensor 7 and (b) position of heat flux sensor 10

Comparing the heat flux and temperature at 1500 W, the temperature difference has a difference of 28.1 percent and the heat flux has a difference of 5.3 percent (fig. 4.16a and fig. 4.16b). In total, heat flux sensor 7 has a deviation of 26.3 percent on heat flux sensor 10. So, the position has no influence on the result. Moreover, the placing of the heat blanket has a significant influence on the results.

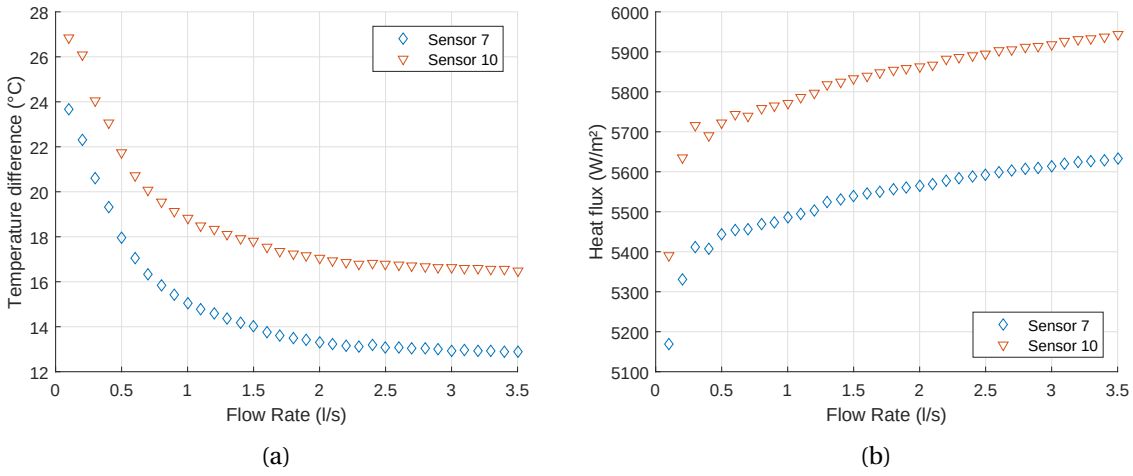

Figure 4.16: Position of heat flux sensor 7 and 10 with thermal paste Arctic Silver 5, thickness respectively 0.05 mm and 0.05 mm, at 1500 W (a) temperature difference from heat flux sensor to inside water and (b) heat flux of heat flux sensor

4.2.4. Variable 4: Honeycomb structure

In the beginning of this section is discussed that the theoretical curve starts at a Reynolds number of 10000. A honeycomb structure is used in the experiments to provide a laminar flow at the lowest flow rates. Figure 4.17 compares the result with and without the honeycomb structure. The influence of the honeycomb structure is visible, but the difference is not as large as expected. Between 0.1 l/s and 0.5 l/s, the experimental data without the honeycomb structure approaches to the theoretic curve more. For this experiment, the heat blanket has not been removed.

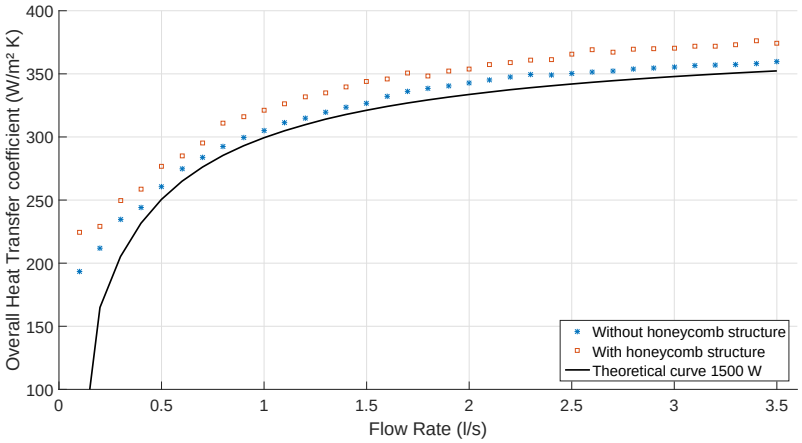

Figure 4.17: Local overall heat transfer coefficient at the position of heat flux sensor 10 with thermal paste Arctic Silver 5, honeycomb structure

4.2.5. Theoretical curve

The theoretical curve for the overall heat transfer coefficient is mainly formed by the convection through water. The other thermal resistance, heat flux sensor, thermal paste and the tube are conductive and did not change for the heat transfer coefficient unless the temperature increases a lot. The heat flux sensor has a maximum temperature of 120 °C and is assumed to be constant. So, when the convection in the water is not taken into account, the maximum theoretical local overall heat transfer coefficient is 380 W m^{-2} K^{-1}. Equation 2.64 of Gnielinski [45] is used to describe the convection in water. The Reynolds and Nusselt number are correlated to each other and given in figure 4.18a. In literature, Sparrow et al. found the same correlation while using a Prandtl number of 2.5 [46]. Plotting the Reynolds number on a logarithmic scale against the Nusselt number on the normal scale, the regime changes in figure 4.18b can be compared with figure 2.8, although the conditions are unequal. Visible is that the Nusselt number from experimental data is not following the equation of Gnielinski at Reynolds 10000 or smaller. The experimental data points are few, so it will only give an indication that the regime becomes transitional.

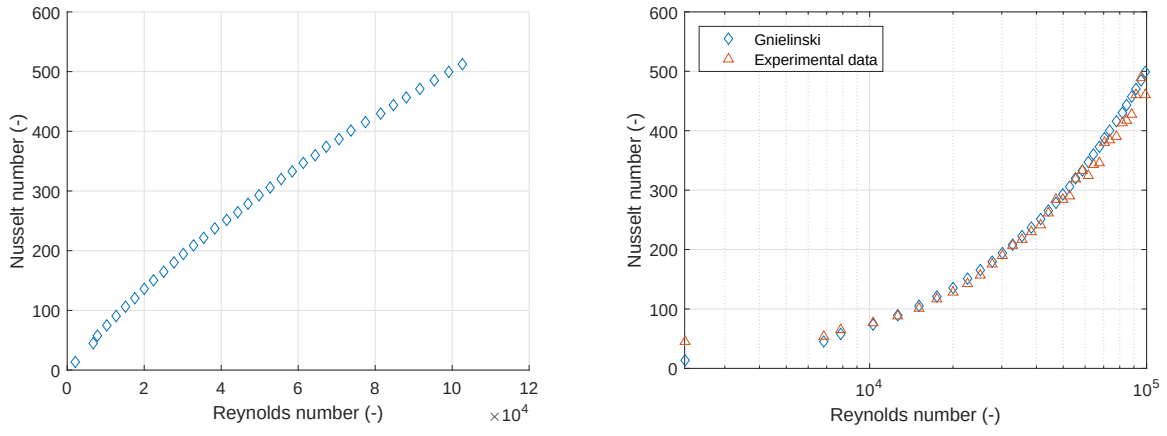

(a) (b)

Figure 4.18: Correlation between Nusselt number and Reynolds number (a) theoretical analyse and can be compared with Sparrow et al. [46] and (b) Gnielinski equation and experimental data on log scale and can be compared with Ndenguma et al. [35]

In table 4.4, the thermal resistances are given for the water to the heat flux sensor. The water varies because the flow rate goes from 0.1 l/s to 3.5 l/s with an increase of temperature.

Table 4.4: Thermal resistance across tube at 1500 W. Resistance of water varies between 0.1 l/s and 3.5 l/s

	Resistance [W m^{-2} K^{-1}]
Water at 0.1 l/s	$7.8 \cdot 10^{-3}$
Water at 3.5 l/s	$0.2 \cdot 10^{-4}$
Tube	$0.7 \cdot 10^{-4}$
Thermal paste	$1.9 \cdot 10^{-4}$
Sensor	$2.6 \cdot 10^{-3}$

For each experimental setup, the tube, thermal paste and sensor can be different. However, the convection of heat through the water is always similar. So, the theoretical convection and the found experimental convection are plotted together. The experimental convection is the temperature difference between the bulk temperature of the water and the temperature at the inside of the wall. The inside temperature of the wall is not measured. This temperature is calculated by deducting the temperature of the heat flux sensor from the resistance to the inside wall of the tube. Knowing the temperature difference and heat flux, the heat transfer has been calculated.

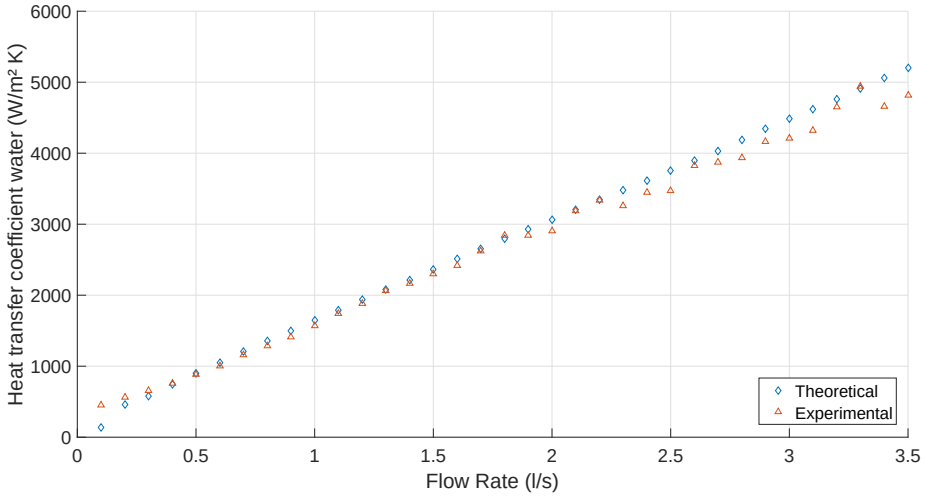

Figure 4.19: Heat transfer coefficient water at 1500 W at position of heat flux sensor 10

In theory, section 2.4.3, there are two methods discussed for calculating the temperature which can be used to determine the correct Nusselt number. To investigate the difference, both are plotted (fig. 4.20a and fig. 4.20b). The difference between both methods is negligible. Which means that the more precise method, with a correction on friction and Nusselt number by the bulk temperature and the surface temperature, is similar to the result of the reference temperature.

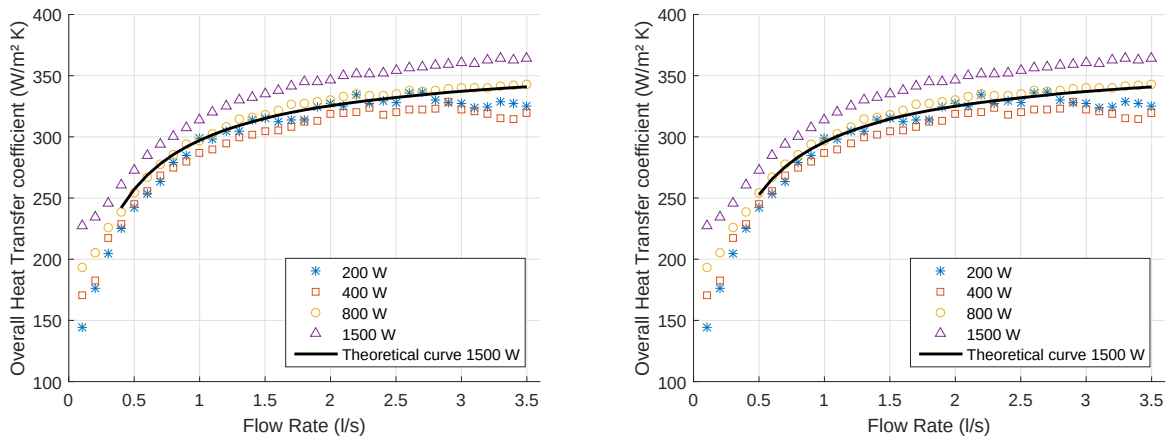

Figure 4.20: Comparison between two methods for the correction of the water temperature in the tube. (a) Method with reference temperature and (b) method with correction on friction factor and Nusselt number

4.2.6. Reliability of experiments

For the reliability of the results, the experimental data must be reproducible. All experiments for the power input, as well as the thermal paste are performed three times. After one performance, the complete installation was cooled and the pump has been shut down so that there is no influence from the previous measurement. For the changing in position and the honeycomb structure, the measurements are done twice. The three measurements with the same power input are given in figure 4.21a with Danfoss 'Koperpasta tube AT' thermal paste at the position of heat flux sensor 10 and figure 4.21b with Arctic Silver 5 thermal paste at the position of heat flux sensor 10. The precision between the different measurements is respectively 0.14 percent and 0.8 percent at 2 l/s.

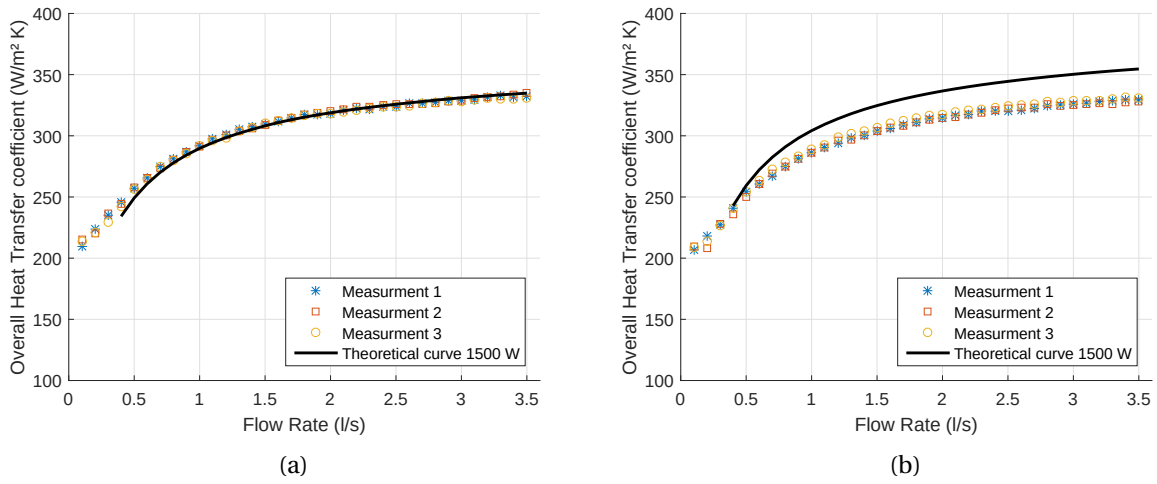

Figure 4.21: Three measurement at position of heat flux sensor 10 with the same power input of 1500 W (a) Thermal paste Danfoss 'Koperpasta tube AT' and (b) Thermal paste Arctic Silver 5

Collecting one data point needs a measuring time of 30 seconds. The time-average is taken, which is given as one point on the diagram. In between the measurements, the flow rate is increased with 0.1 l/s. After that, the time inbetween measurements is 30 seconds. To verify that the process is in steady state again, a test has been done to check the outcome of the measurements. The procedure is as follows: the test begins with a flow rate of 0.2 l/s and increase doubling. The maximum flow rate

reached is 3.2 l/s. After that, the flow rate decreases back from 2.4 l/s to 0.3 l/s. Figure 4.22 shows the results. The experimental data follows the theoretical line, so it can be concluded that the time between the measurements is properly. The theoretical line is not as smooth as the previous shown plots, the temperature and heat flux are used from the measurements to create the theoretical line.

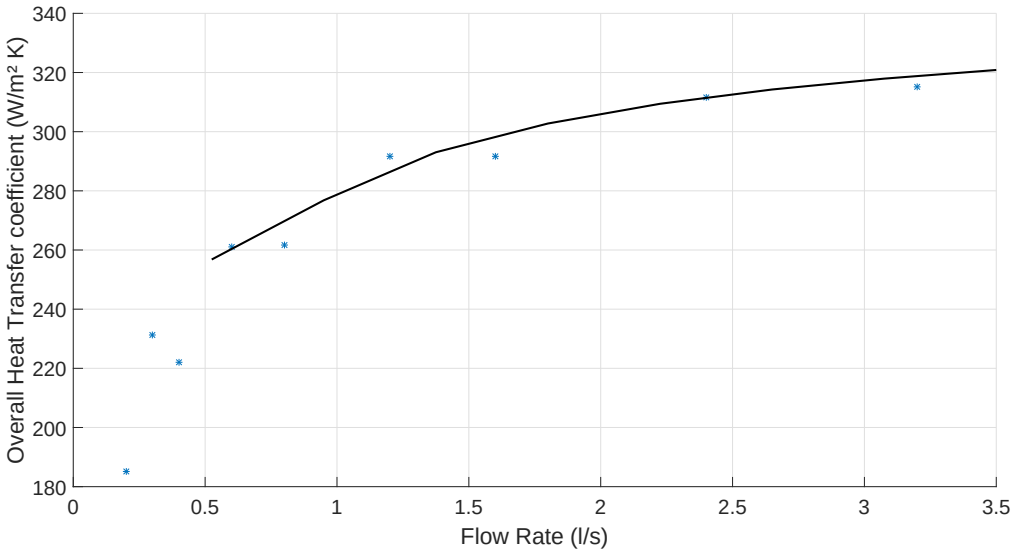

Figure 4.22: Time inbetween measurements is 30 seconds at position of heat flux sensor 10 with a power input of 1500 W and with thermal paste Danfoss 'Koperpasta tube AT'

The precision between the different measurements is shown before in figure 4.21a and figure 4.21b. The temperature sensor used is a type K thermocouple. The error in the thermocouple is generally taken as ± 0.75 percent or maximum ± 2.2 °C [47]. The heat flux sensor has a thermocouple type T for the temperature, with ± 0.75 percent or maximum ± 1 °C. The heat flux has an accuracy of ± 5 percent. All errors are percentage errors because the error is not limited by the temperature limit. For the calculation of the local overall heat transfer coefficient, both temperature and heat flux sensors are used. Uncertainties are added up in quadrature to calculate the error [48]. Not taken into account in the error analysis are the thickness of the tube, paste and sensor. Also, the thermal conductivity of the material is used from the manufacturer. The error is set on measurement two in the diagram (fig. 4.23). Measurement one and three have the same error, however, chosen is to show only measurement two.

The grey area in the diagram is the theoretical error. The error only depends on the equation of Gnielinski, where the error fits in a range of ± 20 percent on most available experimental data. The theoretical error becomes smaller at higher flow rates. This is caused by other resistances, which become increasingly dominant.

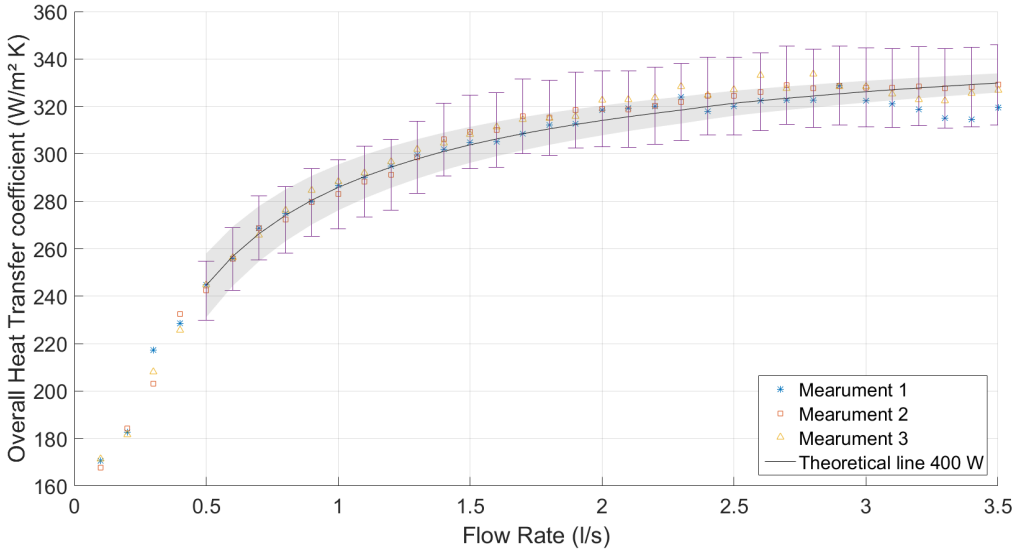

Figure 4.23: Error bar of the measurement at position of heat flux sensor 6, for measurement two. Power input of 400 W and with thermal paste Danfoss 'Koperpasta tube AT'. The grey area in the diagram is the theoretical error.

5

Conclusion

In this report, the falling film in an evaporator has been studied theoretically and the local overall heat transfer coefficient of a tube with a full water flow has been determined experimentally for various configurations. The objective of this research was to determine theoretically the local overall heat transfer coefficient of the falling film and to investigate experimentally the applicability of heat flux sensors by determining the local overall heat transfer coefficient. The local overall heat transfer coefficient contains information about the thickness of the falling film and will detect dry spots as well.

In literature, the falling film evaporator has been extensively studied over the last decades. Multiple aspects are already investigated, such as the efficiency, residence time, vapour flow inside the tube, fouling factor, fluid dynamics of falling film and some estimations about the overall heat transfer coefficient. In June 2017, the first analysis for the heat transfer coefficient of the falling film was presented for a juice evaporator.

From the theoretical analysis of the falling film evaporator it appears that the Reynolds number decreases rapidly in the first 10 meters inside the tube. The kinematic viscosity has the largest influence on the Reynolds number. Concluding from the solid dry mass diagram, the evaporation is almost halfway at 10 meter inside the tube and the kinematic viscosity increased by a factor of 20. The selection of the heat flux sensors depends on the heat flux, which for the falling film evaporator is in the range of 1800 to 30000 W m^{-2}. Among the heat flux, it is important that the heat flux sensors fit on the tube, can resist the maximum temperature and are resistance to water. The heat flux sensor of Fluxteq has been selected.

The overall heat transfer coefficient of a tube filled with water is well-known in literature and therefore the heat flux sensors are investigated under these conditions. Only for flows in the transition regime, there is no generally accepted equation or empirical relations. So, for Reynolds number > 10000, the theoretical curve is valid. Normally, the generally accepted threshold for the Reynolds number by transitional flows is 3000. In this experimental setup, there is a honeycomb structure used which influence the transition point upwards for the laminar flow. This results in a shift upwards for transitional regime as well. The honeycomb structure has been removed to study the difference. No hard conclusion can be drawn, yet it is observed that the curve fits slightly better on the theoretical curve.

Comparing the results, the thermal paste of Danfoss 'Koperpasta tube AT' gives better results than the thermal paste of Arctic Silver 5. Both thermal pastes follow the experimental data curve but the deviation of the Arctic Silver 5 is larger. The influence of the position of the heat flux sensor has been measured as well. The conclusion is that the result is independent of the position of the heat flux sensor. However, the place on that position is important due to the position of the heat blanket.

The heat flux sensor at the entry length with Danfoss 'Koperpasta tube AT' is in good comparison with the theoretical approach and is compared with the entry length described by Mills. The mean difference is the factor used for the Nu_x/Nu_{inf}. Mills uses 1.8, however, for this experimental setup, 1.5 shows a better fit with the experimental data. For the entry length with thermal paste of Arctic Silver 5, the best explanation is that the heat blanket is slightly changed in position due to the fact that the deviation is completely off.

In other experiments, the tube, thermal paste and heat flux sensor can be different. However, the properties of water are constant at the same temperature and pressure. So, the experimental data and the theoretical analysis are compared and both are following the same curve and trend. Only at the lowest flow rate, below the Reynolds number of 10000, a difference appears. This is possibly to the transition regime.

For reliable results, it is important that the experimental data is reproducible. As demonstrated in chapter 4, the measurements have a fluctuation of only 0.14 percent for the Danfoss 'Koperpasta tube AT' and 0.8 percent for Arctic Silver 5 at 2 l/s. The measurement error margin of the local overall heat transfer coefficient stays within the limit boundaries for the thermal paste of Danfoss 'Koperpasta tube AT'.

The local overall heat transfer coefficient of the falling film has been studied and the mass flow per unit width of {700, 900, 1100} kg m^{-1} h^{-1} are investigated. The error margin of the used sensors in the experimental setup, over the overall heat transfer coefficient at 900 kg m^{-1} h^{-1}, 10 meter into the tube, is 47.6 W m^{-2} K^{-1}. The difference of overall heat transfer coefficient between 700 kg m^{-1} h^{-1} and 900 kg m^{-1} h^{-1} is 140 W m^{-2} K^{-1}. From the experimental setup with full flow of water can be concluded that the thermal paste of Danfoss 'Koperpasta tube AT' gives results within the predicted error margin. So, the conclusion is that the heat flux sensors are applicable for the use of the falling film evaporator.

6

Recommendations

In further research work, the theoretical analysis of the falling film evaporator as well as the experimental results can be improved to gain better results.

For the theoretical analysis, the vapour flow inside the tube and the film of the condensation are not taken into account in this research. The falling film inside the tube depends on the vapour flow in the core of the tube. The velocity of this vapour flow is in contact with the surface of the falling film which can result in a more turbulent falling film. However, relative high velocities of vapour flow may cause surface instabilities which can break the falling film and cause dry spots or droplets. The condensation of steam on the outside of the tube will lead to a falling film. The steam on the outside of the tube, used for the heating of the tubes, has the same influence on the falling film, created from the condensation of the steam on the tube, as the vapour flow inside the tube. The only difference is that the steam evaporates the liquid of the film during the fall. All these factors have influence on the local overall heat transfer coefficient. To analyse these factors, it is recommended to perform a computational fluid dynamics simulation.

For the experimental result, the full water flow has been studied and compared with the theory. However, the falling film with water can be implemented in this setup as well. By doing so, the final use of the heat flux sensors can be investigated. Furthermore, more constant results will be obtained when the heat blanket is replaced by a heat blanket which has a homogeneous distribution of heat. So, the question if the heat blanket is positioned exactly as the previous measurement is not relevant anymore. The second improvement to the setup is the temperature sensors above and below the heat blanket. Since the temperature difference is small, it would be preferable to have more sensitive temperature sensors. Furthermore, when the heat flux sensors in combination with the falling film with water has been extensively investigated, the transition regime between wavy laminar and turbulent can be investigated as well.

A

Heat flux sensor specification

In table A.1, the specification of the heat flux sensor Fluxteq PHFS-01e is given. The heat flux sensor measure the heat flux as well as the temperature.

Table A.1: Heat flux sensor Fluxteq [49]

Sensor Type	Differential-Temperature Thermopile
Encapsulation Material	Copper
Nominal Sensitivity	Approx. 9.0 mV cm^2 W^{-1}
Sensor Thickness	Approx. 600 microns
Specific Thermal Resistivity	Approx. 0.9 K m^2 kW^{-1}
Absolute PHFS Thermal Resistance	Approx. 1 K W^{-1}
Heat Flux Range	± 150 kW m^{-2}
Temperature Range	- 50 °C to 120 °C
Response Time	Approx. 0.9 seconds
Sensor Surface Thermocouple	Type-T
Sensing Area Dimensions	2.54 x 2.54 cm
Total Sensor Dimensions	3 x 3.2 cm
Sensing Area	6.45 cm^2
Total Sensor Area	9.6 cm^2

The heat flux sensor is shown below:

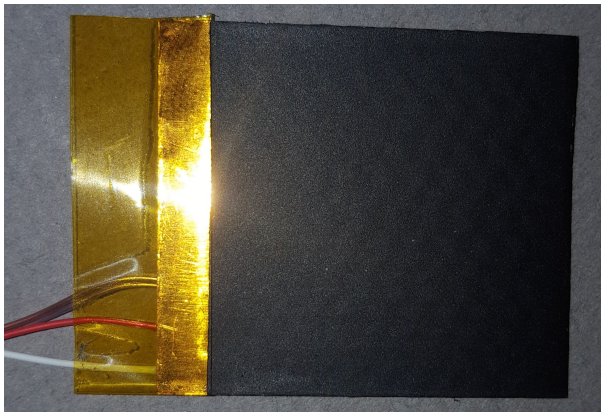

Figure A.1: Heat flux sensor

Bibliography

[1] O. F. Hunziker. *Condensed Milk and Milk Powder*. La Grange, Illinous,The author,. https://www.biodiversitylibrary.org/bibliography/29694.

[2] Milk Spray Dryers Dairy Spray Dryer whey Spray Dry lactose Spray Drying. http://www.dairyconsultant.co.uk/milk_spray_dryers_drying.php.

[3] Dairy: World Markets and Trade | USDA Foreign Agricultural Service. https://www.fas.usda.gov/data/dairy-world-markets-and-trade.

[4] M. T. Munir, Y. Zhang, D. I. Wilson, W. Yu, B. R. Young, and S. Street. Modelling of a Falling Film Evaporator for Dairy Processes. page 8, 2014.

[5] Falling Film Evaporator. http://www.gea.com/nl/products/falling-film-evaporator.jsp.

[6] M. Gourdon, F. Innings, A. Jongsma, and L. Vamling. Qualitative investigation of the flow behaviour during falling film evaporation of a dairy product. *Experimental Thermal and Fluid Science*, 60:9–19, January 2015. ISSN 08941777. doi: 10.1016/j.expthermflusci.2014.07.017.

[7] J. A. Winchester and C. Marsh. Dynamics and Control of Falling Film Evaporators with Mechanical Vapour Recompression. *Chemical Engineering Research and Design*, 77(5):357–371, July 1999. ISSN 0263-8762. doi: 10.1205/026387699526340.

[8] M. T. Munir, W. Yu, and B. R. Young. Can Exergy be a Useful Tool for the Dairy Industry? In J. J. Klemeš, P. S. Varbanov, and P. Y. Liew, editors, *Computer Aided Chemical Engineering*, volume 33 of *24 European Symposium on Computer Aided Process Engineering*, pages 1129–1134. Elsevier, January 2014. doi: 10.1016/B978-0-444-63455-9.50023-4.

[9] Q. Ruan, H. Jiang, M. Nian, and Z. Yan. Mathematical modeling and simulation of countercurrent multiple effect evaporation for fruit juice concentration. *Journal of Food Engineering*, 146: 243–251, February 2015. ISSN 0260-8774. doi: 10.1016/j.jfoodeng.2014.09.015.

[10] Y. Zhang, M. T. Munir, I. Udugama, W. Yu, and B. R. Young. Modelling of a milk powder falling film evaporator for predicting process trends and comparison of energy consumption. *Journal of Food Engineering*, 225:26–33, May 2018. ISSN 0260-8774. doi: 10.1016/j.jfoodeng.2018.01.016.

[11] A. C. P. Silveira, G. Tanguy, Í. T. Perrone, R. Jeantet, F. Ducept, A. F. de Carvalho, and P. Schuck. Flow regime assessment in falling film evaporators using residence time distribution functions. *Journal of Food Engineering*, 160:65–76, September 2015. ISSN 0260-8774. doi: 10.1016/j.jfoodeng.2015.03.016.

[12] M. Chun and S. Park. Effects of turbulence model and interfacial shear on heat transfer in turbulent falling liquid films. *International Communications in Heat and Mass Transfer*, 22(1): 1–12, January 1995. ISSN 0735-1933. doi: 10.1016/0735-1933(94)00047-O.

[13] W. Li, X. Wu, Z. Luo, and R. L. Webb. Falling water film evaporation on newly-designed enhanced tube bundles. *International Journal of Heat and Mass Transfer*, 54(13):2990–2997, June 2011. ISSN 0017-9310. doi: 10.1016/j.ijheatmasstransfer.2011.02.052.

[14] C. O. Díaz-Ovalle, G. González-Alatorre, and J. F. J. Alvarado. Analysis of the dynamic response of falling-film evaporators considering fouling. *Food and Bioproducts Processing*, 104:124–136, July 2017. ISSN 0960-3085. doi: 10.1016/j.fbp.2017.05.007.

[15] P. Cyklis. Industrial scale engineering estimation of the heat transfer in falling film juice evaporators. *Applied Thermal Engineering*, 123:1365–1373, August 2017. ISSN 1359-4311. doi: 10.1016/j.applthermaleng.2017.05.194.

[16] VDI-Gesellschaft Verfahrenstechnik und Chemieingenieurwesen, editor. *VDI Heat Atlas*. VDI-buch. Springer, Berlin ; New York, 2nd ed edition, 2010. ISBN 978-3-540-77876-9. OCLC: ocn489638163.

[17] K. R. Morison, J. P. Phelan, and C. G. Bloore. Viscosity and Non-Newtonian Behaviour of Concentrated Milk and Cream. *International Journal of Food Properties*, 16(4):882–894, May 2013. ISSN 1094-2912. doi: 10.1080/10942912.2011.573113.

[18] R. P. Chhabra and J. F. Richardson. Chapter 1 - Non-Newtonian Fluid Behaviour. In *Non-Newtonian Flow and Applied Rheology (Second Edition)*, pages 1–55. Butterworth-Heinemann, Oxford, 2008. ISBN 978-0-7506-8532-0. doi: 10.1016/B978-0-7506-8532-0.00001-9.

[19] R. Numrich. Heat transfer in turbulent falling films. *Chemical Engineering & Technology*, 18(3): 171–177, June 1995. ISSN 0930-7516, 1521-4125. doi: 10.1002/ceat.270180305.

[20] R. S. Jebson and M. Iyer. Performances of falling film evaporators. *Journal of Dairy Research*, 58(01):29, February 1991. ISSN 0022-0299, 1469-7629. doi: 10.1017/S0022029900033483.

[21] R. S. Jebson and H. Chen. Performances of falling film evaporators on whole milk and a comparison with performance on skim milk. *Journal of Dairy Research*, 64(1):57–67, February 1997. ISSN 00220299. doi: 10.1017/S0022029996001963.

[22] A. C. P. Silveira, A. F. de Carvalho, Í. T. Perrone, L. Fromont, S. Méjean, G. Tanguy, R. Jeantet, and P. Schuck. Pilot-scale investigation of effectiveness of evaporation of skim milk compared to water. *Dairy Science & Technology*, 93(4-5):537–549, July 2013. ISSN 1958-5586, 1958-5594. doi: 10.1007/s13594-013-0138-1.

[23] A. F. Mills. *Basic Heat and Mass Transfer*. Pearson Education Limited, second edition edition, 2014. ISBN 1-292-04248-6.

[24] J. Fourier. Analytical theory of heat. 1878.

[25] Incropera, De Witt, Bergman, and Lavine. *Fundamentals of Heat and Mass Transfer*. Wiley, sixth edition edition. ISBN 978-0-471-45728-2.

[26] M. I. Davidzon. Newton's law of cooling and its interpretation. *International Journal of Heat and Mass Transfer*, 55(21-22):5397–5402, October 2012. ISSN 00179310. doi: 10.1016/j.ijheatmasstransfer.2012.03.035.

[27] V. V. Guzanov, A. V. Bobylev, O. M. Heinz, S. M. Kharlamov, A. Z. Kvon, and D. M. Markovich. Characterization of 3-D wave flow regimes on falling liquid films. *International Journal of Multiphase Flow*, 99:474–484, February 2018. ISSN 0301-9322. doi: 10.1016/j.ijmultiphaseflow.2017.11.013.

[28] M. Gourdon, E. Karlsson, F. Innings, A. Jongsma, and L. Vamling. Heat transfer for falling film evaporation of industrially relevant fluids up to very high Prandtl numbers. *Heat and Mass Transfer*, 52(2):379–391, February 2016. ISSN 0947-7411, 1432-1181. doi: 10.1007/s00231-015-1556-9.

[29] Dimensionless Numbers. https://www.iist.ac.in/sites/default/files/people/numbers.html.

[30] K. R. Chun and R. A. Seban. Heat Transfer to Evaporating Liquid Films. *Journal of Heat Transfer*, 93(4):391–396, November 1971. ISSN 0022-1481. doi: 10.1115/1.3449836.

[31] F. M. White. *Fluid Mechanics*. Mc Graw Hill, New York, seventhh edition edition, 2011.

[32] L.P.B.M. Janssen and M.M.C.G. Warmoeskerken. *Transport Phenomena Data Companion*. VSSD, Delft, third edition edition, 2006. ISBN 978-90-71301-59-9.

[33] E. M. Sparrow, T. M. Hallman, and R. Siegel. Turbulent heat transfer in the thermal entrance region of a pipe with uniform heat flux. *Applied Scientific Research*, 7(1):37–52, January 1957. ISSN 0003-6994. doi: 10.1007/BF03184700.

[34] S. Kakaç, R. K. Shah, and W. Aung. *Handbook of Single-Phase Convective Heat Transfer*, volume Chapter 3. Wiley, New York, 1987. ISBN 978-0-471-81702-4. OCLC: 15198221.

[35] D. D. Ndenguma, J. Dirker, and J. P. Meyer. Heat transfer and pressure drop in annuli with approximately uniform internal wall temperatures in the transitional flow regime. *International Journal of Heat and Mass Transfer*, 111:429–441, August 2017. ISSN 0017-9310. doi: 10.1016/j.ijheatmasstransfer.2017.02.064.

[36] B. O. Hasan. Heat transfer analysis in thermal entrance region under turbulent flow conditions. *Asia-Pacific Journal of Chemical Engineering*, 8(4):578–592, July 2013. ISSN 1932-2143. doi: 10.1002/apj.1698.

[37] A. F. Mills. Experimental Investigation of Turbulent Heat Transfer in the Entrance Region of a Circular Conduit. *Journal of Mechanical Engineering Science*, 4(1):63–77, March 1962. ISSN 0022-2542, 2058-3389. doi: 10.1243/JMES_JOUR_1962_004_010_02.

[38] McAdams and H. Williams. Heat transmission. (3rd), 1954.

[39] S. K. Singh, M. K. Yadav, and S. Khandekar. Measurement issues associated with surface mounting of thermopile heat flux sensors. *Applied Thermal Engineering*, 114:1105–1113, March 2017. ISSN 1359-4311. doi: 10.1016/j.applthermaleng.2016.12.076.

[40] A. S. Sabau and Z. Wu. Evaluation of a heat flux sensor for spray cooling for the die casting processes. *Journal of Materials Processing Technology*, 182(1):312–318, February 2007. ISSN 0924-0136. doi: 10.1016/j.jmatprotec.2006.07.039.

[41] A. W. Van Herwaarden and P. M. Sarro. Thermal sensors based on the seebeck effect. *Sensors and Actuators*, 10(3):321–346, November 1986. ISSN 0250-6874. doi: 10.1016/0250-6874(86)80053-1.

[42] Armaflex Armacell. Technische gegevens - AF/Armaflex. page 4.

[43] S. W. Churchill and M. Bernstein. A Correlating Equation for Forced Convection From Gases and Liquids to a Circular Cylinder in Crossflow. *Journal of Heat Transfer*, 99(2):300–306, May 1977. ISSN 0022-1481. doi: 10.1115/1.3450685.

[44] Pumica N - Pull Rhenen - Thermisch. http://www.pullrhenen.nl/thermisch/en/pumica_k/pumica_n.html.

[45] V. Gnielinski. New equations for heat and mass transfer in turbulent pipe and channel flow. 16: 359–368, 1976.

[46] E. M. Sparrow and M. M. Ohadi. Numerical and Experimental Studies of Turbulent Heat Transfer in a Tube. *Numerical Heat Transfer*, 11(4):461–476, April 1987. ISSN 0149-5720. doi: 10.1080/10407788708913565.

[47] Type K Thermocouple. Thermocouple Type K | Type K Thermocouple | Chromel/Alumel Thermocouple. http://www.thermometricscorp.com/thertypk.html.

[48] A summary of Error Propagation. http://ipl.physics.harvard.edu/wp-uploads/2013/03/PS3_Error_Propagation_sp13.pdf.

[49] FluxTeq Heat Flux Sensors | National Lab-Approved Heat Flux Sensors | PHFS-01e Heat Flux Sensor. http://www.fluxteq.com/phfs-01e-heat-flux-sensor.